*nanomaterials*

MDPI

*Review*

# 2D Material and Perovskite Heterostructure for Optoelectronic Applications

**Sijia Miao [1], Tianle Liu [1], Yujian Du [2], Xinyi Zhou [1], Jingnan Gao [1], Yichu Xie [1], Fengyi Shen [1], Yihua Liu [1] and Yuljae Cho [1,*]**

[1] UM-SJTU Joint Institute, Shanghai Jiao Tong University, Shanghai 200240, China; sijia_miao@sjtu.edu.cn (S.M.); tyrion_l2017@sjtu.edu.cn (T.L.); zxylily@umich.edu (X.Z.); gjn0310@sjtu.edu.cn (J.G.); xieyichu@umich.edu (Y.X.); 1517511250@sjtu.edu.cn (F.S.); ayka_tsuzuki@sjtu.edu.cn (Y.L.)

[2] School of Microelectronics, Dalian University of Technology, Dalian 116620, China; imduke@mail.dlut.edu.cn

* Correspondence: yuljae.cho@sjtu.edu.cn

**Abstract:** Optoelectronic devices are key building blocks for sustainable energy, imaging applications, and optical communications in modern society. Two-dimensional materials and perovskites have been considered promising candidates in this research area due to their fascinating material properties. Despite the significant progress achieved in the past decades, challenges still remain to further improve the performance of devices based on 2D materials or perovskites and to solve stability issues for their reliability. Recently, a novel concept of 2D material/perovskite heterostructure has demonstrated remarkable achievements by taking advantage of both materials. The diverse fabrication techniques and large families of 2D materials and perovskites open up great opportunities for structure modification, interface engineering, and composition tuning in state-of-the-art optoelectronics. In this review, we present comprehensive information on the synthesis methods, material properties of 2D materials and perovskites, and the research progress of optoelectronic devices, particularly solar cells and photodetectors which are based on 2D materials, perovskites, and 2D material/perovskite heterostructures with future perspectives.

**Keywords:** 2D materials; perovskites; heterostructures; optoelectronics

check for updates

**Citation:** Miao, S.; Liu, T.; Du, Y.; Zhou, X.; Gao, J.; Xie, Y.; Shen, F.; Liu, Y.; Cho, Y. 2D Material and Perovskite Heterostructure for Optoelectronic Applications. *Nanomaterials* **2022**, *12*, 2100. https://doi.org/10.3390/nano12122100

Academic Editor: Jun-ho Yum

Received: 2 May 2022
Accepted: 16 June 2022
Published: 18 June 2022

**Publisher's Note:** MDPI stays neutral with regard to jurisdictional claims in published maps and institutional affiliations.

**Copyright:** © 2022 by the authors. Licensee MDPI, Basel, Switzerland. This article is an open access article distributed under the terms and conditions of the Creative Commons Attribution (CC BY) license (https://creativecommons.org/licenses/by/4.0/).

## 1. Introduction

As modern technology improves by leaps and bounds, optoelectronic devices, such as solar cells and photodetectors, have become indispensable parts of society. These semiconductor devices that convert optical signals into electrical ones have wide applications in the areas of renewable energy, imaging systems, biomedical devices, and optical communications [1–4]. Over the past few decades, tremendous efforts have been made persistently to enhance the efficiency and stability of the devices through synthesizing high-quality materials [5–12], designing novel device structures, engineering interfaces [13], and employing encapsulation with polymer and inorganic glass [14,15].

2D materials, including graphene and its derivatives, transition metal dichalcogenides (TMDCs), and black phosphorous (BP), have attracted intense interest in optoelectronic applications due to their distinctive optical, electrical, and mechanical characteristics [12,16–20]. These nanomaterials possess strong in-plane covalent bonds whereas each layer is vertically connected by weak van der Waals (vdWs) force. The unique vdWs structures enable the exfoliation of an ultrathin single layer with a uniformly distributed thickness and orientation [21–24]. Despite the great potential of 2D materials in advanced optoelectronics, their atomic-scale thickness largely restricts the light absorption capacity of devices, resulting in unsatisfactory device performance [25].

Meanwhile, perovskites have been regarded as a promising active layer in high-performance optoelectronic devices. Since the first demonstration of perovskite solar cells

with a power conversion efficiency (PCE) of 3.8% in 2009 [26], the record PCE has been elevated to over 25% till now [27], almost catching up with commercial photovoltaic applications [26,27]. Similarly, perovskite-based photodetectors have also achieved impressive progress, with the champion device exhibiting detectivity exceeding $10^{14}$ Jones and fast response speed at the nanosecond level [28,29]. The outstanding performance of perovskite devices mainly stemmed from their fascinating properties, such as high light absorption coefficient, adjustable bandgap, and long charge carrier diffusion length [30,31]. However, challenges still remain regarding the long-term stability issues and unsatisfactory interfaces, which require further intensive research [5,6,32].

Recently, the integration of 2D materials and perovskites for heterostructures has stimulated a research hotspot. The heterostructures enable the absorption of more photons and enhanced resistance to moisture and oxygen by combining the advantages of both materials, bringing more opportunities for future optoelectronic industries. In addition, some 2D materials are found to be superior alternatives for carrier transport layers [13,33]. In light of this, it is of importance to review comprehensive aspects including the materials, devices, and integration technology of 2D materials and perovskites.

In this regard, we present comprehensive information on the applications of 2D materials, perovskites, and 2D material/perovskite heterostructures for applications to solar cells and photodetectors. We begin with an introduction to the synthesis methods and basic properties of 2D materials and perovskites. Then, we summarize the development of optoelectronic devices based on 2D materials and perovskites and address the existing issues. Further, we introduce the newly-emerged concept of 2D material/perovskite heterostructure and its impressive progress in optoelectronics. We focus on the synergistic effects of integrating these materials and the underlying mechanisms of performance enhancement. Finally, we discuss the remaining challenges of developing stable, high-quality, and environmentally friendly 2D material/perovskite heterostructures.

## 2. Synthesis of 2D Materials

### *2.1. Graphene and Its Derivatives*

Graphene is one atomic layer of graphite with a thickness of approximately 0.35 nm and has attracted lots of interest from academia and industries due to its excellent properties, such as a theoretical specific surface area (2630 $m^2$ $g^{-1}$), optical transparency, intrinsic mobility (200,000 $cm^2$ $V^{-1}$ $s^{-1}$), Young's modulus (~1.0 TPa) and thermal conductivity (~5000 W $m^{-1}$ $K^{-1}$) [12,16,17,34]. Ever since its first demonstration, tremendous efforts have been put into its synthesis [21]. Among various methods to synthesize graphene, we will introduce mechanical exfoliation, liquid exfoliation, and chemical vapor deposition (CVD), which are commonly used.

#### 2.1.1. Mechanical Exfoliation

Graphene was believed not to exist in the free state until Geim and Novoselov obtained it via mechanical exfoliation in 2004 [21]. The thin flakes of graphite could be successively cleaved into thinner flakes using adhesive tapes down to a single atomic layer (Figure 1a). The crystallinity of the obtained flakes was high and further examinations confirmed the anomalous quantum Hall effect which was predicted by Semenoff [35–37]. These observations not only showed the great potential of graphene as a platform for studying quantum physics, kicking off the race in this field but also yielded a Nobel prize. However, the mechanical exfoliation was inefficient in producing a large volume of graphene and the size obtained was limited.

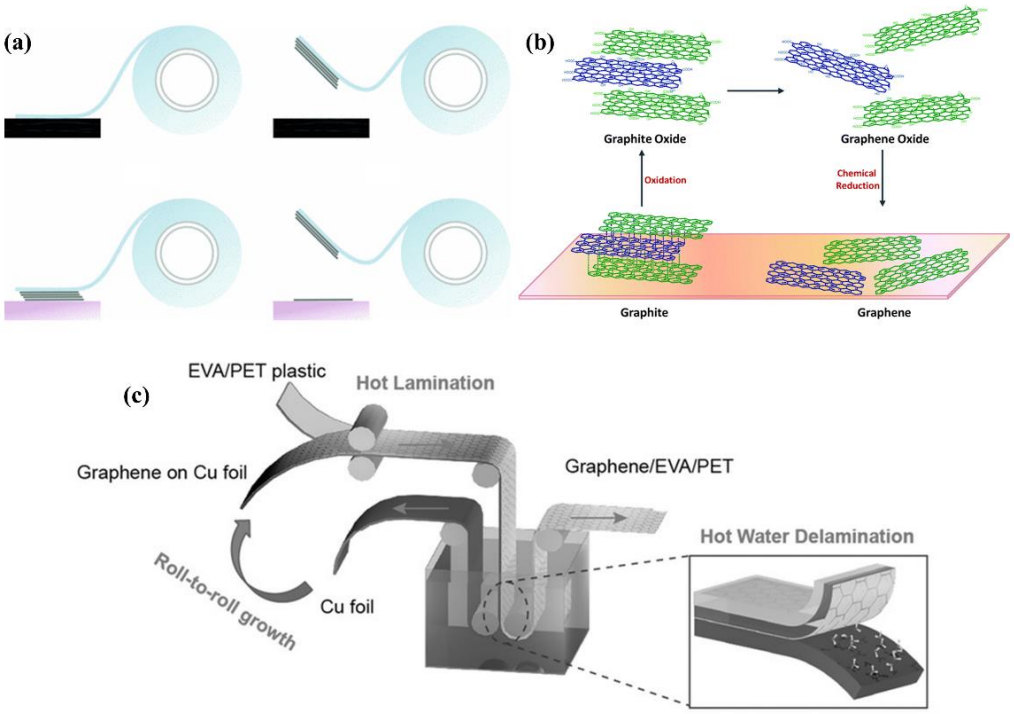


**Figure 1.** (**a**) Schematics of mechanical exfoliation method [38]; (**b**) Schematic of chemical exfoliation method [39]; (**c**) Schematic of roll-to-roll production of graphene from a Cu foil to a target substrate [40]. (**a**) Reprinted with permission from Ref. [38]. Copyright 2011, WILEY. (**b**) Reprinted with permission from Ref. [39]. Copyright 2014, RSC. (**c**) Reprinted with permission from Ref. [40]. Copyright 2015, WILEY.

#### 2.1.2. Chemical Exfoliation

Since graphene tends to aggregate in commonly available solvents, researchers have developed the chemical exfoliation method. In this method, graphite is first oxidized to introduce hydrophilic functional groups, such as carboxyl, hydroxyl, and epoxide groups, and then dispersed in water via sonication. The dispersed solution is finally reduced to graphene by thermal annealing or by using chemical reagents (Figure 1b) [39]. Therefore, graphene synthesized in this way is termed reduced graphene oxide (rGO). Typically, $KMnO_4$, $NaNO_3$, and a strong acid (e.g., $H_2SO_4$) are used as an oxidizer. This synthesis route developed by Hummers is safer compared with $KClO_3$ used initially. Later, other researchers modified Hummers' method by using various reduction agents, such as hydrohalic acids, aluminum hydride, and sodium ammonia [41–43]. Chemical exfoliation is cost-effective and scalable. However, the method introduces defects in graphene in the oxidation process, which degrades properties such as electron mobility and thermal conductivity.

#### 2.1.3. Chemical Vapor Deposition

The CVD of graphene is typically performed on copper or nickel through a thermal method. Methane is a commonly used carbon source. As it is exposed to the heated metal surface, the metal catalyzes the loss of hydrogen and dissolves the remaining carbon, leading to a layer of metal carbide [12]. As the temperature drops, the metal carbide surface layers saturate, and graphitic carbon precipitates out. In this way, large-area single-layer graphene can be obtained. Though researchers have known for a long time that the CVD of hydrocarbon on metals can generate thin graphite layers, the breakthrough of CVD for graphene did not occur until self-limiting graphene growth on Cu was discovered in 2009 [44]. Since the graphene growth was irrelevant to the thickness of Cu foil and C solubility in Cu was very low, the proposed mechanism for the self-limiting growth was surface-catalysis rather than precipitation during cooling. In addition, patterned

graphene could be obtained by patterning the metal substrate used for growth, which offers huge benefits in patterning graphene after the synthesis [45]. Remarkably, a large area of graphene was also successfully attained by the roll-to-roll process for flexible transparent electrodes (Figure 1c) [40,46].

### *2.2. 2D Transition Metal Dichalcogenides*

2D transition metal dichalcogenides (TMDCs), such as $MoS_2$, $MoSe_2$, and $WS_2$, have gained great attention because they show properties different from their bulk counterparts [10]. For example, the $MoS_2$ monolayer is a direct bandgap semiconductor while the bulk crystal is an indirect one with a narrower bandgap. Thus, monolayer $MoS_2$ shows much stronger photoluminescence than the multiple layers. Among various methods, we will introduce mechanical exfoliation, liquid exfoliation, and chemical vapor deposition, which are the most widely used methods to synthesize 2D TMDCs [22,23,47–49].

#### 2.2.1. Mechanical Exfoliation

After the successful demonstration of mechanical exfoliation of graphene, it has been extended to 2D TMDCs as well. Typically, an adhesive tape is used to peel off a thin layer from a bulk crystal, and then the layer is transferred to a target substrate, leaving single or multiple layers of TMDCs on the substrate [38,50]. Although mechanical exfoliation provides nanosheets with clean surfaces and a good crystallinity, it is not scalable and does not have systematic control over layer size and thickness. The layers mechanically exfoliated are typically of several microns size. To obtain larger layers, Magda and coworkers employed the chemical affinity of S atoms to Au to achieve $MoS_2$ single layers of several hundred microns size on Au (111) surfaces [22]. Furthermore, they found that their method could be extended to other chalcogenides, such as $WSe_2$ and $Bi_2Te_3$ as well.

#### 2.2.2. Liquid Exfoliation

Liquid exfoliation is another popular method to fabricate 2D TMDCs which can be further categorized as solvent intercalation, chemical intercalation, and electrochemical intercalation (Figure 2a,b) [49,51,52]. It typically yields nanosheets with small lateral sizes (<1 μm) which tend to aggregate upon deposition. The main idea behind the method is to weaken the vdWs interaction between layers to separate them. Organolithium is commonly used for chemical intercalation (Figure 2a). However, in the case of $MoS_2$, the as-exfoliated nanosheets showed a dominant metastable metallic phase rather than a semiconducting phase due to Li intercalation. Eda and coworkers found that mild annealing at 300 °C led to the gradual restoration of the semiconducting phase [20].

It is also viable to exfoliate single TMDC layers through direct sonication in organic solvents or solvent intercalation (Figure 2a). Coleman et al. tested various organic solvents in many TMDCs ($MoS_2$, $MoSe_2$, $WS_2$, etc.) and found *N*-methyl-pyrrolidone (NMP) and isopropanol (IPA) resulted in stable dispersions [53]. However, the yield was low and the dispersion also contained multilayer TMDCs.

In order to improve the yield and obtain better control over the intercalation process, Zeng et al. developed the electrochemical intercalation method (Figure 2b) [49]. A bulk TMDC was incorporated as a cathode of a test cell while a Li foil was used as an anode to provide intercalation ions. Hence, the degree of intercalation could be controlled in the discharge process, leading to a 92% yield of single-layer TMDC.

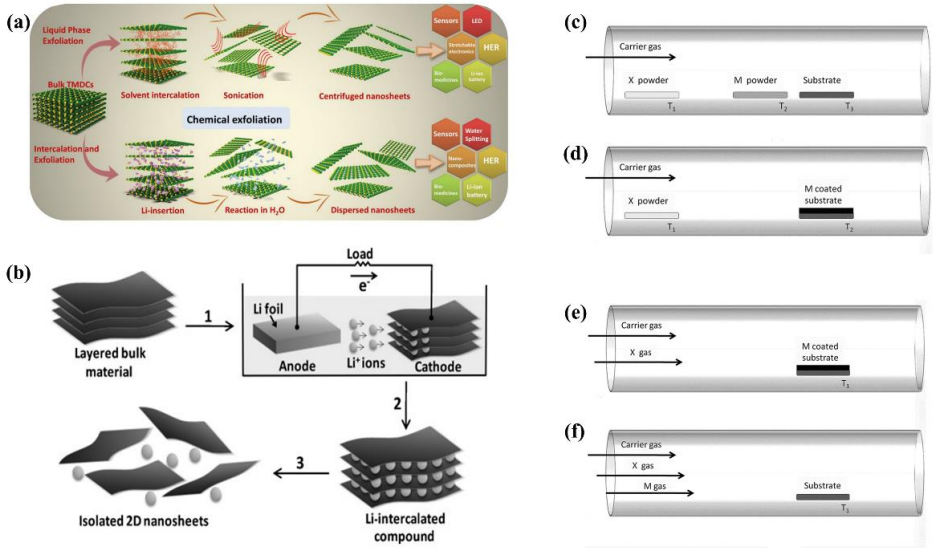


**Figure 2.** (**a**,**b**) Different liquid exfoliation mechanisms: (**a**) solvent intercalation, and chemical intercalation [52], and (**b**) electrochemical intercalation [49]; (**c**–**f**) Chemical vapor deposition setups depending on the precursors [47]. (**a**) Reprinted with permission from Ref. [52]. Copyright 2021, WILEY. (**b**) Reprinted with permission from Ref. [49]. Copyright 2019, RSC. (**c**–**f**) Reprinted with permission from Ref. [47]. Copyright 2015, RSC.

### 2.2.3. Chemical Vapor Deposition

CVD is the most widely used bottom-up technology in fabricating atomically thin TMDCs. As a well-developed technique, it has better control of synthesis parameters and is, therefore, able to produce large-area monolayer TMDCs. Various precursors can be used as metal and chalcogen sources, such as $MoO_3$, $WO_3$, Se powder, and $H_2S$ [47,54–56]. For the CVD method, a different experimental setup needs to be adopted depending on the types of sources (Figure 2c–f). Figure 2c shows the setup for metal and chalcogen sources in powders. Since evaporation of metal (or metal oxides) and synthesis of TMDC require a temperature much higher than the boiling point of chalcogen powders, it is important to control the furnace temperature profile. When the metal has a very high boiling temperature (e.g., tungsten), its oxide (e.g., $WO_3$) is usually used instead [55]. When Se is used, $H_2$ in the carrier gas is usually required as a reducing agent [56]. During the synthesis, seeding promoters can also be applied to avoid unwanted structures, such as nanorods and nanoparticles.

TMDC monolayers can also be synthesized through the chalcogenization of metal or metal oxide deposited on the substrate (Figure 2d,e). The thickness of the metal or metal oxide layer is about 1–5 nm and determines the number of TMDC layers [57]. Hence, the difficulty of this method lies in the precise control of thickness and homogeneity of the pre-deposited layer over a large area. Figure 2f illustrates the setup when both metal and chalcogenide sources are in the gas phase. Common precursors are $Mo(CO)_6$, $W(CO)_6$, $H_2S$, and dimethyl disulfide (DMDS) [47]. In the case of $Mo(CO)_6$ and dimethyl disulfide (DMDS) forming $MoS_2$, the reaction can happen at low temperatures (100–140 °C), but the resulted nanosheets require subsequent annealing at 900 °C to obtain a better crystallinity [58].

## 3. Synthesis of Lead Halide Perovskites

Lead halide perovskites (LHPs) with a chemical formula $ABX_3$ (B = Pb and X = Cl, Br, or I) are promising materials in optoelectronic applications due to their high defect tolerance, large light absorption coefficients, and long charge carrier diffusion length. According to the requirement for ionic radii, there are only three suitable cations in cubic α-phase, namely, cesium ($Cs^+$), methylammounium ($MA^+$), and formamidium ($FA^+$) ions. These materials have been applied in various optoelectronics such as solar cells, light-emitting diodes (LEDs), and photodetectors [59–61]. However, bulk perovskites are unstable under

ambient atmosphere and irradiation, which triggers studies on their more stable reduced-dimensional counterparts, namely 0D quantum dots, 2D, and quasi-2D. Comprehensive reviews on the synthesis of perovskites can be found in [5–9,62,63], and therefore we summarize the synthesis methods of perovskites with different dimensions for optoelectronic applications in this review.

### *3.1. 3D Lead Halide Perovskites*

For 3D LHPs, tremendous efforts have been made in engineering materials' stability and morphology in order to fully utilize outstanding materials properties which were overshadowed by the poor air stability and film morphology. Among various film deposition methods, here we focus on the most common approaches, namely, two-step sequential deposition, one-step spin-coating, and thermal evaporation (Figure 3a,b). Various strategies have been explored in the frame of those methods to stabilize LHPs and improve the quality of films, such as mixing A-site cations and X-site anions, and adding organic molecules or lower dimensional LHP to passivate surfaces and grain boundaries [61,64,65].

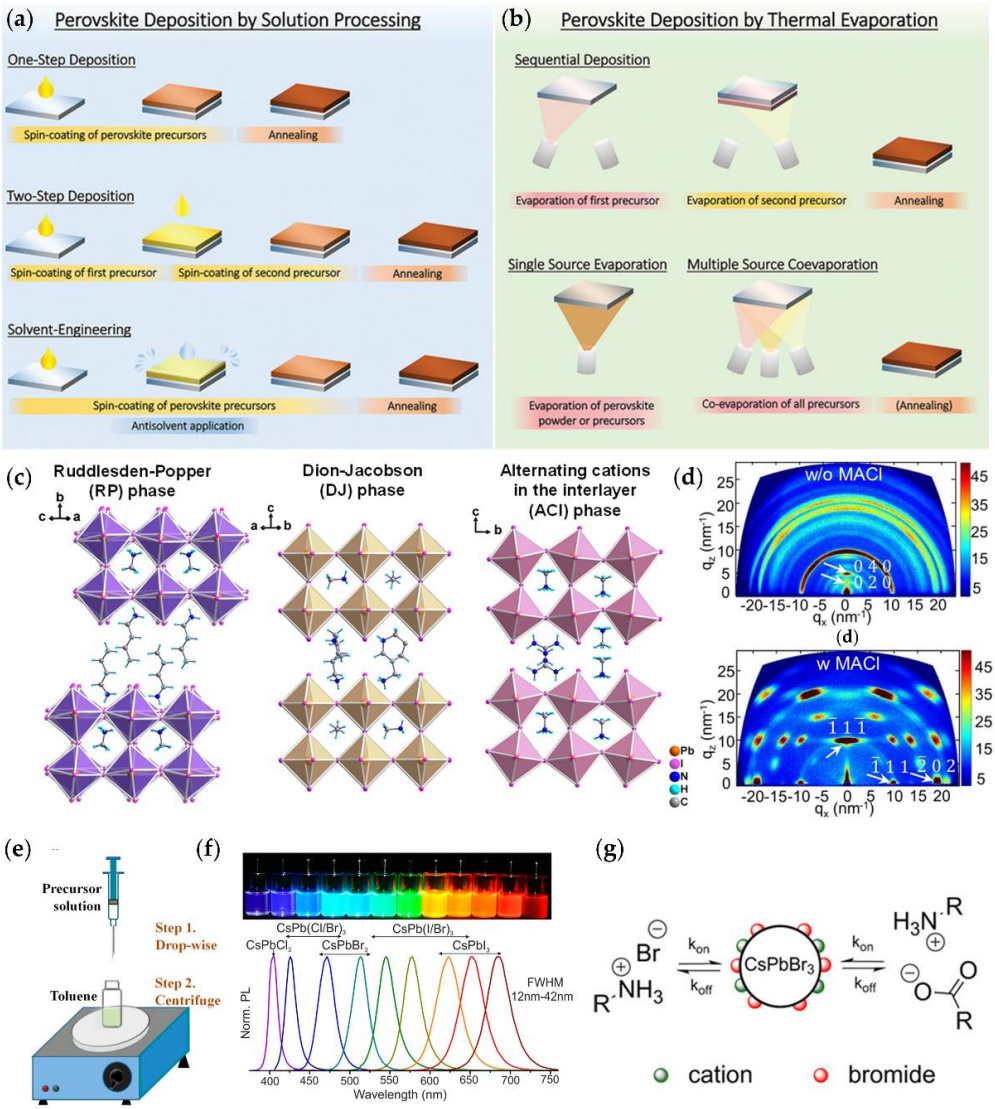


**Figure 3.** (**a**) Schematic illustration of one-step, two-step sequential, and antisolvent method for 3D LHP film deposition [63]; (**b**) Schematic illustration of single-source, sequential, and multi-source thermal evaporation [63]; (**c**) Examples showing structures of RP, DJ, and ACI phases of <100>-oriented LHP respectively [7]; (**d**) Grazing-incident wide-angle X-ray scattering patterns of

(PXD)$(MA)_2Pb_3I_{10}$ with and without MACl additive [66]; (**e**) Schematic presentation of the LARP method [67]; (**f**) $CsPbX_3$ PQDs in toluene under UV lamp (365 nm) and the normalized PL spectra [68]; (**g**) Schematic representation of the dynamic ligand binding of OA and OAm to PQD surfaces [69]. (**a**,**b**) Reprinted with permission from Ref. [63]. Copyright 2020, WILEY. (**c**) Reprinted with permission from Ref. [7]. Copyright 2021, ACS. (**d**) Reprinted with permission from Ref. [66]. Copyright 2020, WILEY. (**e**) Reprinted with permission from Ref. [70]. Copyright 2015, ACS. (**f**) Reprinted with permission from Ref. [68]. Copyright 2015, ACS. (**g**) Reprinted with permission from Ref. [69]. Copyright 2016, ACS.

The two-step sequential deposition was one of the widely used methods in the early age of perovskite research for 3D LHP films [63]. Typically, an inorganic layer, for example, $PbI_2$, is first spin-coated on a substrate, and then the deposited inorganic layer is immersed into an organic salt solution, for example, methylammonium iodide (MAI). Alternatively, the organic salt solution is spin-coated on the inorganic layer to form the desired 3D LHPs (Figure 3a). For the two-step sequential deposition methods, it is important to control parameters to obtain the high-quality film, such as the morphology of the inorganic layer at the first step, the concentration of the organic salt solution, and the speed of the spin-coating [62]. Although the two-step method offers good reproducibility and compact films, it often encounters an issue of incomplete conversion. This has resulted from the formation of perovskite on the surface of the inorganic layer which inhibits the diffusion of organic cations. Gong et al. introduced nickel chloride ($NiCl_2$) as an additive in the $PbI_2$ precursor to form a porous film [71]. As a result, the MAI solution could penetrate the $PbI_2$ film more easily, leading to the formation of larger perovskite grains. Engineering solvents have also been introduced as another strategy. Zhi and coworkers added *N*-Methyl-2-pyrrolidone (NMP) with low volatility to the MAI precursor to assist the recrystallization process of the 3D LHPs and to enhance Ostwald ripening, resulting in films with large columnar grains [72].

3D LHP films can also be fabricated via a one-step spin-coating method. In this method, all the components are dissolved in the same solvent to form a precursor and spin-coated generally at two stages, such as at a low speed for a short time and then at a high speed for a long time (Figure 3a). However, the resultant films could have pinholes, rough surfaces, and small grains. To resolve these issues, additives can incorporated in precursors before spin-coating. Lewis acids (e.g., iodopentafluorobenzene) or bases (e.g., methylammonium chloride (MACl)) are commonly used to passivate under-coordinated halide or Pb atoms at grain boundaries or surfaces, while other additives like $Pb(SCN)_2$ are shown to improve the crystallinity and grain size of 3D LHPs [5,73,74]. Another approach is to drip antisolvent on substrates at the second stage of spin-coating to facilitate homogeneous nucleation by extracting the host solvent (Figure 3a). A wide range of antisolvent has been employed, from highly polar ethyl acetate to nonpolar toluene, from diethyl ether with a low boiling point to chlorobenzene with a high boiling point [75–78]. According to Taylor and coworkers, the application of the antisolvent is not instantaneous and its duration is also an important factor [79].

Other than the spin-coating method, thermal evaporation is another film deposition method widely employed. The evaporation method can be further categorized as a single-source, sequential, and multisource co-deposition (Figure 3b) [63]. In the single-source thermal evaporation, either the prepared perovskite powder or the mixed precursor is put in one crucible for the thermal evaporation. In the sequential evaporation, the individual precursor is evaporated separately, followed by a thermal or vapor annealing. The most common method is the multisource co-evaporation where each precursor is placed in different crucibles and evaporated at the same time. The thermal evaporation method is suitable for large-scale fabrication and conformal films. It also allows precursors with solvent orthogonality and prevents damaging underlying layers during deposition. However, there are drawbacks to thermal evaporation as well. It requires expensive and complex vacuum systems, which limits the number of studies. The grain size of thermally evaporated films is typically smaller than that of the solution-processed films. Lohmann et al. found that as the substrate temperature

decreased from room temperature to −2 °C, the grain size of $MAPbI_3$ increased from 100 nm to micrometer size [80]. However, it has also been pointed out that the evaporation of MAI is difficult to control due to its relatively high vapor pressure and low decomposition temperature [81]. To solve this problem, vapor-deposited MA-free perovskite films have been studied. For instance, Lohmann and coworkers showed that partially substituting $PbCl_2$ for $PbI_2$ could significantly suppress defects in $FA_{0.83}Cs_{0.17}PbI_3$ films [82].

The deposition methods mentioned above aim at fabricating films with uniform and full coverage. However, sometimes localized crystallization and patterned films are preferred. A laser-assisted crystallization method shows advantages in this sense. Arciniegas et al. demonstrated confined growth of $MAPbBr_3$ via laser irradiation [83]. The growth mechanism was ascribed to the local generation of MA ions from the *N*-methylformamide solvent due to laser-induced heat. In addition to crystal growth, laser irradiation could also lead to a reversible localized phase transition. Zou and coworkers illustrated a nonvolatile rewritable photomemory array based on this principle [84].

### *3.2. 2D and Quasi-2D Lead Halide Perovskites*

(Quasi-)2D LHPs can be seen as a slice cleaved from an ideal cubic perovskite along certain crystalline planes, such as <100> by layers of organic ions [7,85]. Therefore, they can be categorized according to the cleaving planes and the thickness of the inorganic layers between the organic spacers. <100>-oriented (quasi-)2D LHPs have a chemical formula $A'_2A_{n-1}Pb_nX_{3n+1}$ or $A'A_{n-1}Pb_nX_{3n+1}$ (A′ = 1+ or 2+, A = 1+ cation, X = Cl, Br, or I) and can be further classified as: (i) Ruddlesden-Popper (RP) phase, (ii) Dion-Jacobson (DJ) phase, and (iii) alternating cation in the interlayer space (ACI) phase (Figure. 3c). All three phases consist of inorganic layers of corner-sharing $[PbX_6]^{4-}$ octahedrons. The difference between these phases lies in the stacking displacement of adjacent layers. The RP phase is characterized by the interdigitated organic bilayer which causes the inorganic layers staggered by half a unit cell (0.5, 0.5 in-plane displacement). The DJ phase features a perfect stacking (0, 0 in-plane displacement) and bivalent organic cation spacers. In the ACI phase, A-site cations not only appear in the cuboctahedral cages but also alternate with the spacers in the organic layer. Many linear monoammonium cations, such as butylammonium, pentylammonium, and hexylammonium, can adopt RP structures [86]. DJ phase is usually derived from diammonium spacers, including both linear types like $NH_3C_mH_{2m}NH_3$ ($m$ = 7−9) and cyclic types like 3-(aminomethyl)piperidinium (3AMP) and 1,5-naphthalene diammonium [85,87,88]. However, unlike RP and DJ phases, ACI structure can only be templated by guanidinium (GUA) currently [70].

All three phases of (quasi-)2D LHP show a conductivity in the stacking direction much lower than the in-plane directions because the organic cations act as barriers. As a result, excitons are confined in the inorganic slabs, showing a binding energy depending on the n value. Therefore, red shifts in absorption and emission spectra are observed as n increases. Although the electrical and optical properties of the three phases are similar in general, there are still some differences. DJ (quasi-)2D LHPs usually show a smaller bandgap than RP ones with the same n value due to less distortion in inorganic layers and a shorter interlayer distance [89]. In addition, DJ (quasi-)2D LHPs are more stable than RP ones [8,90]. Although the hydrophobic property of the spacers in the RP phase provides resistance to humidity, the vdWs gap in the bilayer made the devices vulnerable when being subjected to high temperature and high humidity at the same time. The hydrogen-bonding interaction in the DJ phase is stronger than the vdWs interaction in the RP phase and therefore leads to a more rigid and tight structure, providing better device stability.

For the synthesis of (quasi-)2D LHPs as a device component, a spin-coating method with a precursor is more frequently used, resulting in a multicrystalline film [70,85,91]. The precursor can be made by dissolving individual components in an organic solvent. For optoelectronic applications, the (quasi-)2D LHP layer usually consists of grains with random orientations. As the organic spacers inhibit charge transport along the stacking direction, a crystal orientation with organic layers perpendicular to the substrate is preferred

in devices. Various additives, such as $NH_4SCN$, $Pb(SCN)_2$, and MACl, have been applied to the precursor to form crystals with vertically aligned organic layers [66,92,93]. It is proposed that the additives function by suppressing the formation of $PbI_2$ sol-gel which acts as nucleation sites and tends to transform into an unoriented intermediate phase [94]. Currently, grazing-incident wide-angle X-ray scattering is the most widely used tool to characterize the crystal orientation. The diffraction pattern will be a Scherrer ring if the grains are randomly oriented, and bright spots if vertically oriented (Figure 3d) [66].

In addition to random crystal orientation, the 2D LHP layer is typically composed of phases with different *n* values. Since the bandgap of 2D LHP decreases as n increases, the distribution of *n* values would cause excitons to funnel to domains with large *n* values [95]. Ma and coworkers designed a bifunctional molecular additive, tris(4- fluorophenyl)phosphine oxide (TFPPO), to narrow down the *n*-value distribution and passivate the lateral sides of 2D LHP at the same time. The *n*-value distribution was ascribed to the slower diffusion of organic spacers due to hydrogen bonds formed between the spacer's ammonium tails and the fluorine atoms in TFPPO [96].

A thin 2D LHP layer can also be deposited on a 3D LHP film to form a 2D/3D heterostructure by spin-coating a solution containing organic spacers on the 3D LHP film [97–99]. The resultant 2D LHP layer is typically a couple of nanometers thick and consists of phases with $n = 1$ or 2. Although the large bandgap and exciton binding energy of low *n* values are unfavorable in solar cells, the 2D LHP layers provided passivation to the surface of 3D LHP film and therefore improved the stability and open-circuit voltage. Typically, IPA is used as the solvent for organic spacers due to the good solubility it offers. Additional halide compounds, such as potassium iodide (KI) and rubidium iodide (RbI), may also be added to the solution [100]. However, IPA can also dissolve the underlying 3D LHP layer due to its strong polarity, leading to a 3D/2D mixed phase at the surface. To obtain a clear heterojunction, Yoo et al. employed chloroform (CF) as the solvent for the organic spacers to avoid damaging the underlying 3D LHP film [101]. However, only certain linear ammonium halide, for example, n-hexylammonium bromide, showed solubility high enough to be applied in the spin-coating method. To overcome the conflict in the solution process, Jang and coworkers developed a solid-phase in-plane growth method to synthesize an intact and clear 2D/3D junction with control over the thickness of the 2D layer [102]. A 2D LHP film and a 3D LHP film were deposited on two substrates separately via the single-step spin-coating method. After the two films were stacked in contact, heat and pressure were applied to induce the growth of the 2D layer on the 3D film. Finally, the substrate with 2D LHP solid precursor was detached, leaving an intact 2D layer on the 3D LHP film. The thickness of the 2D layer could be controlled by adjusting the temperature or performing the process iteratively.

### *3.3. 0D Lead Halide Perovskite Quantum Dots*

Perovskite quantum dots (PQDs) not only inherit excellent optical and electronic properties from LHPs but also show unique advantages, such as size-tunable bandgaps, and high photoluminescence quantum yield (PLQY). PQDs are typically synthesized through a solution method. However, they may also form in inorganic glass with the aid of laser irradiation. For example, Huang et al. demonstrated the laser-induced in-situ formation of $CsPbBr_3$ quantum dot in an inorganic oxide glass which enabled 3D patterning [103]. The pattern could be erased by thermal annealing and rewritten by laser irradiation many times. Below we introduce two main solution synthesis methods for PQDs: ligand-assisted reprecipitation (LARP) and hot injection where the hot injection method is mostly employed to synthesize high-quality PQDs.

#### 3.3.1. Ligand Assisted Reprecipitation

Generally, organic-inorganic hybrid PQDs are synthesized via the LARP method whereas the hot injection method is used more frequently for all inorganic PQDs. Schmidt et al. first reported the spherical $CH_3NH_3PbBr_3$ ($MAPbBr_3$) PQDs synthesized by a precipitation method

at room temperature [104]. The PQDs showed a green emission (~525 nm) with a narrow FWHM (~25 nm) and PLQY of 20%. Later, PLQY was improved to 83% by changing the molar ratio of reactants [105]. Zhang et al. modified the precipitation method by using capping ligands (octylamine and oleic acid) to limit the growth of crystals and named it LARP (Figure 3e) [67]. A precursor with capping ligands in a good solvent (e.g., DMF) was drop-wisely added to a bad solvent (e.g., toluene). The authors concluded that octylamine controlled the kinetics of crystallization and consequently the size of PQDs, while OA prevented aggregation and therefore enhanced stability. However, organic-inorganic hybrid PQDs synthesized by the LARP method were still less stable than their all-inorganic counterpart, such as $CsPbX_3$ PQDs, due to the volatile organic component, especially when exposed to heat and moisture.

#### 3.3.2. Hot Injection

Hot injection synthesis of PQDs was first performed by L. Protesescu et al. motivated by reports on hybrid organic-inorganic metal halide perovskite [68]. A Cs-oleate stock solution was injected into a lead halide ($PbX_2$) precursor at 140–200 °C to form monodispersed cubic-shape PQDs of different sizes (4–15 nm). Various halide compositions could be readily achieved by adjusting the ratio in $PbX_2$ precursor, such as $PbI_2$:$PbBr_2$ = 1:1 and $PbBr_2$:$PbCl_2$ = 1:1. The composition and quantum confinement effect due to sizes gave $CsPbX_3$ PQDs a tunable bandgap covering the entire visible spectral region (Figure 3f). The all-inorganic PQDs also showed a large charge carrier mobility (4500 $cm^2$ $V^{-1}$ $s^{-1}$), high PLQY, and narrow full with half maximum (FWHM), which made them attractive in optoelectronic applications, such as solar cells, photodetectors, and LEDs [106–112]. Later, Protesescu et al. also reported a fast anion exchange in $CsPbX_3$ which provided a post-synthesis method to finely tune the composition [113]. The fast exchange was attributed to the well-known high anion conductivity in bulk halide perovskite and the highly dynamic ligand binding of the PQDs (Figure 3g) [69]. However, the easy loss of capping ligands also made it difficult to maintain PQDs intact during a purification process. Swarnkar et al. found that methyl acetate (MeOAc) was a suitable antisolvent to isolate $CsPbI_3$ PQDs while keeping the integrity [112]. Unlike their bulk counterpart which quickly transferred to an orthorhombic phase at room temperature, the densely packed PQD film was stable in a cubic $\alpha$-phase for months under ambient conditions due to the large surface area and high surface energy of PQDs. Although MeOAc maintained PQDs intact during purification, there were still surface defects formed, such as iodine vacancy, while removing surface ligands. Recently, Jia et al. tackled the problem by adding tert-butyl iodide (TBI) and trioctylphosphine (TOP) in the purification process [114]. The iodine ions released from the nucleophilic substitution reaction between TBI and TOP cured the surface defects. In addition to purification methods, researchers have optimized other synthesis parameters, such as the ratio of different precursors, reaction temperatures, solvents, and capping ligands [115–120].

For PQDs, ligand exchange is necessary to fabricate efficient devices, as the long organic ligands used in synthesis significantly block the charge transfer. A two-step solid-state ligand exchange is widely performed by dipping the PQD film in methyl acetate and ethyl acetate ligand solutions subsequently [121–123]. In this way, OA/OAm capping ligands can be changed into acetic acid/FA or other short ligands to facilitate electric coupling between PQDs. However, ligand exchange may cause more defects on QD surfaces, and therefore a post-treatment with cesium salts is needed to passivate those defects [124]. Furthermore, FA cations are hygroscopic and able to enter PQDs, which results in device instability. To overcome the drawbacks of using the FA cations and enhance the device stability, other large hydrophobic cations such as phenylethylammonium (PEA) and GUA have been explored [125,126].

## 4. 2D Materials for Optoelectronic Applications

2D materials, such as graphene, TMDCs, and BP, have attracted tremendous research interest in the field of optoelectronics due to their facile processing techniques and unique properties arising from vdWs structures [33]. For instance, graphene shows ultrafast carrier dynamics and a broad absorption band. TMDCs are favored for their direct bandgap, high light absorption, natural abundance, and excellent chemical stability. Besides, their mechanical flexibility and durability allow the formation of high-quality interfaces with a low density of charge traps [127]. BP has high carrier mobility and a moderated bandgap of around 0.3 eV in its single-layer form, which enables reduced dark current and low noise in photodetection [128]. In this part, we present the recent development of 2D material-based optoelectronics.

### *4.1. 2D Material Solar Cells*

One of the $MoS_2$-based solar cells was proposed by Wi et al. [127]. In the work, the author treated the surface of the $MoS_2$ layer with $CHF_3$ plasma to form a p-n junction in the solar cell (Figure 4a). As illustrated in Figure 4b, the built-in potential between the plasma-treated $MoS_2$ and untreated $MoS_2$ layer could enhance the separation and collection of photogenerated carriers, resulting in improved device performance. The device showed a high current density of 20.9 mA/cm$^2$ and PCE of 2.8%. $WSe_2$ has also shown its potential as a solar cell material in the work reported by McVay et al. [129]. The $WSe_2$ layer was passivated with $Al_2O_3$ and the solar cell demonstrated remarkable photocurrent enhancement (Figure 4c). The passivation layer not only reduced surface traps but also induced n-type surface doping and band bending at the interface, increasing the active area for photocurrent extraction. The fabricated device exhibited a $V_{oc}$ of 380 mV and $J_{sc}$ of 10.7 mA/cm$^2$. In addition, Nazif et al. proposed a flexible solar cell consisting of the $WS_2$ absorbing layer, graphene top contact, and $MoO_x$ coating (Figure 4d) [130]. The transparent graphene top contacts greatly reduced Fermi-level pinning at the interface of TMDC and metal contacts. Additionally, $MoO_x$ served as effective passivation and anti-reflection layer, leading to increased $J_{sc}$. As a result of these strategies, the device exhibited remarkable performance enhancement, with a PCE of 5.1% and specific power of 4.4 W/g in comparison with that of the previously reported counterpart (PCE ~0.7%, specific power ~0.04 W/g). The device performance of solar cells reviewed in Section 4.1 is summarized in Table 1.

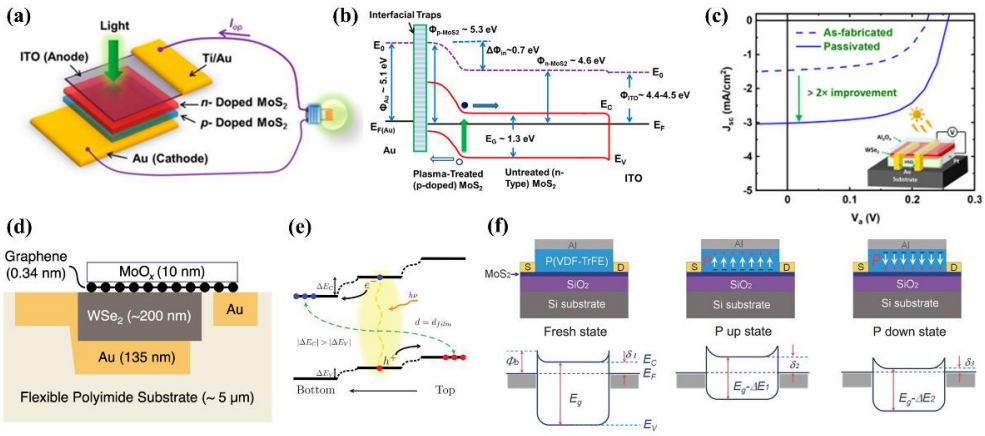


**Figure 4.** (**a**) Schematic of the plasma-treated $MoS_2$ solar cell. (**b**) Energy band level of the plasma-treated $MoS_2$ solar cell. (**c**) The performance improvement of the solar cell passivated by $Al_2O_3$ under a 3400 K black body source of 30 mW/cm$^2$. (**d**) Cross-sectional image of the $MoO_x$/graphene/$WSe_2$ solar cell. (**e**) Energy band diagram of the strain-gradient $WS_2$ film. (**f**) The schematic and energy band diagram of the $MoS_2$ device under different polarization states. (**a**,**b**) Reprinted with permission from Ref. [127]. Copyright 2014, ACS. (**c**) Reprinted with permission from Ref. [129]. Copyright 2020, ACS. (**d**) Reprinted with permission from Ref. [130]. Copyright 2021, Springer Nature. (**f**) Reprinted with permission from Ref. [131]. Copyright 2015, WILEY. (**e**) Reprinted with permission from Ref. [132]. Copyright 2021, Wiley.

**Table 1.** Summarized device performance of solar cells in Section 4.1.

| Active Materials | Voc (V) | Jsc (mA/cm$^2$) | FF (%) | PCE (%) | Ref. |
|---|---|---|---|---|---|
| $MoS_2$ | 0.28 | 20.9 | 47 | 2.8 | [127] |
| $WSe_2$ | 0.38 | 10.7 | 44 | 1.6 | [129] |
| $WS_2$ | 0.476 | 17.3 | 61.7 | 5.1 | [130] |

### *4.2. 2D Material Photodetectors*

#### 4.2.1. Graphene

Ever since the successful exfoliation, graphene has been widely applied to photodetector applications. Here, we summarize significant works based on graphene. First, a graphene photodetector was integrated into a silicon bus waveguide, demonstrating a chip-integrated photodetector technology based on graphene [133]. The coupling strategy in the work greatly improved the light absorption capability of the graphene layer over a broadband spectrum. As a result, the photodetector achieved maximum responsivity of over 0.1 A/W and uniform photoresponse ranging from 1450 to 1590 nm. Second, Kim et al. fabricated a photodetector based on an all-graphene p-n junction [134]. Attributed to the carrier multiplication induced by impact ionization and high photoconductive gain in the graphene layers, the device demonstrated high detectivity (~$10^{12}$ Jones) and photoresponsivity (0.4–1.0 A/W) from ultraviolet to near-infrared region. However, due to the emergence of TMDCs, graphene was substituted with TMDCs for photodetector applications.

In recent years, waveguide-integrated graphene photodetectors have been proposed for datacom applications. Schuler et al. used a silicon photonic waveguide to guide the light in a confined graphene area to facilitate light-matter interaction [135]. The device showed a responsivity of 0.17 A/W. Following this work, Ma et al. demonstrated a graphene photodetector coupled with a silicon waveguide, and arrayed metallic structures were introduced into the device structure to improve the responsivity by exciting surface plasmon polaritons [136]. As a result, the device exhibited an external efficiency of 0.5 A/W with an ultrahigh-frequency response over 110 GHz. Similarly, Alaloul et al. reported a CMOS-compatible graphene photodetector with a plasmon-enhanced responsivity of 1.4 A/W and broad bandwidth exceeding 100 GHz [137].

#### 4.2.2. Transition Metal Dichalcogenides

To date, various TMDCs have been applied for the photodetectors, such as $WS_2$, $MoTe_2$, and $MoS_2$ [138]. For example, $WS_2$ TMDC has attracted tremendous interest as the photodetector material attributed to its availability in both n- and p-type. $WS_2$ is intrinsically an n-type semiconductor, but through doping p-type $WS_2$ can be readily attained. Kim et al. introduced a gradient-strained $WS_2$ film, which was controlled by the sputtering time of W, for the photodetector application [132]. Due to the band edge variation resulting from the gradient strain, a type II homojunction was formed in the multilayer film which effectively reduced nonradiative recombination (Figure 4e). The photodetector demonstrated high photoresponsivity under white light irradiation with a low driven voltage of 0.1 V.

Similarly, Mo-based TMDCs, such as $MoS_2$ and $MoTe_2$, are intrinsically an n-type TMDC with availability in a p-type as well. Particularly, $MoTe_2$ has a suitable bandgap for both visible and near-infrared light photodetection [139,140]. Therefore, a broadband photodetector was introduced by employing the $MoTe_2$ TMDC [141]. The device exhibited high detectivity of $3.1 \times 10^9$ and $1.3 \times 10^9$ Jones for 637 and 1060 nm light, respectively. The authors attributed the high device performance to the photogating effect. The photogenerated holes were localized within the trap states, leading to high photoconductive gain. In addition, Wang et al. developed a $MoS_2$-based photodetector with P(VDF-TrFE) as the ferroelectric gate [131]. The ferroelectric material provided an ultrahigh electrostatic field of about $10^9$ V/m in the semiconducting channel and helped the device maintain a depleted state, significantly suppressing the dark current (Figure 4f). As a result, the

device showed broadband photodetection from 0.85–1.55 μm, as well as high detectivity of $2.2 \times 10^{12}$ Jones and responsivity of 2570 A/W.

#### 4.2.3. Black Phosphorus

BP, a layered semiconducting material similar in appearance to graphite, has risen as a new family member of 2D materials since its first successful exfoliation in 2014. BP has brought new concepts and applications to the field of optoelectronics due to its unique structure and properties. Particularly, BP has the infrared bandgap which offers great potential for IR detection [142]. For example, a mid-infrared photodetector based on BP was demonstrated by Guo et al. [128]. The photodetector exhibited a wide range of operating wavelengths from 532 nm to 3.39 μm. The device showed responsivity of 82 A/W at 3.39 μm and was capable of detecting picowatt light owing to its high photoconductive gain and low dark current. Moreover, the photodetector had effective photoresponse in the kilohertz frequency range due to the carrier dynamics of BP with a moderate bandgap. In addition, Jalaei et al. reported a Se-doped BP photodetector with high responsivity ranging from 3 to 5 μm [143]. Se-doped BP showed smaller bandgap as well as higher absorption coefficient in the mid-infrared region compared to the pristine BP. As a result, the device exhibited responsivity of 0.75 μA/W at 4 μm with the light intensity of 0.0001 W/cm$^2$.

Despite the great progress in optoelectronics using 2D materials as active layers, the majority of devices exhibited unsatisfactory performance mainly due to the poor light absorption limited by their atomic-scale thickness. To resolve this issue, heterostructures were introduced and this structure improved the light absorption capacity, which will be discussed in Part 6 [144]. The device performance of photodetectors reviewed in Section 4.2 is summarized in Table 2.

**Table 2.** Summarized device performance of photodetectors in Section 4.2.

| Active Materials | Response Range | R (A/W) | D* (Jones) | $\tau_{rise}/\tau_{fall}$ | Ref. |
|---|---|---|---|---|---|
| Graphene | 1450–1590 nm | 0.108 | - | - | [133] |
| Graphene | UV-NIR | ~1 | $10^{12}$ | - | [134] |
| Graphene | - | 0.17 | - | - | [135] |
| Graphene | 1480–1620 nm | 0.5 | - | - | [136] |
| Graphene | - | 1.4 | - | 50 μs/- | [137] |
| $WS_2$ | 440–800 nm | 30 | - | - | [132] |
| $MoTe_2$ | 600–1550 nm | 0.05 | $3.1 \times 10^9$ | 1.6 ms/1.3 ms | [141] |
| $MoS_2$ | 500–1550 nm | 2570 | $2.2 \times 10^{12}$ | 1.8 ms/2 ms | [131] |
| BP | 0.532–3.39 μm | 82 | - | - | [128] |
| BP | MIR | $7.5 \times 10^{-7}$ | - | - | [143] |

## 5. Perovskite Optoelectronic Applications

### *5.1. Lead Halide Perovskite Solar Cells*

#### 5.1.1. 3D Lead Halide Perovskite

In two decades, 3D LHP solar cells have made rapid progress and are almost catching up with the PCE of Si-based types. The record PCE of 3D perovskite in a solar cell is 25.6% while a Si-based cell is 26.1%, making perovskite an attractive material for solar cell applications. The first report on 3D LHP solar cells dates back to 2009 by Kojima et al. The device exhibited a PCE of 3.8% using $MAPbI_3$ as the active layer. [26] Following this work, in 2012, Kim et al. reported a high-efficiency solar cell with a PCE of 9.7% based on the structure of mesoporous $TiO_2/MAPbI_3$/spiro-OMeTAD [145]. In the same year, Lee et al. employed mesoporous alumina as an insulating scaffold for the $MAPbI_2Cl$ perovskite and achieved a solar cell with a PCE of 10.9% and low energy losses [146]. Due to high PCEs achieved in a short period, these two findings have attracted intense research interest in perovskite solar cells and greatly facilitated the development of this area.

In 2013, a two-step sequential deposition method was introduced for the formation of $MAPbI_3$ perovskite layer in solar cells, which opened a new route for high-performance

solution-processed perovskite solar cells [147]. $PbI_2$ dissolved in DMF solution was spin-coated on the $TiO_2$ underlayer, and then the substrate was dipped into the MAI solution. This led to $PbI_2$ being transformed into the 3D LHP with a greatly improved film morphology compared to the conventional one-step deposition approach. Attributed to the improved morphology, the device exhibited a high PCE of 15%. Similarly, Yang et al. deposited a $PbI_2$ (DMSO) complex in a DMF solution on the $TiO_2$ layer, followed by the spin-coating of the FAI solution [148]. $FAPbI_3$ crystallization occurred through the intramolecular exchange process (IEP) of DMSO with FAI. According to SEM and XRD results, the perovskite film by the IEP method showed a smoother surface, larger grain size, and better (111)-preferred crystal orientation in comparison with its counterpart by the conventional method. Benefiting from this technique, over 20% of PCE was achieved in 3D perovskite solar cells.

In 2015, Bi et al. reported high-quality $MAPbI_3$ perovskite layers grown on non-wetting HTLs with a thickness aspect ratio of 2.3–7.9 [149]. Non-wetting HTLs reduced the surface tension dragging force compared to wetting HTLs, which increased the grain boundary mobility, yielding the growth of larger perovskite grains with improved crystallinity. As a result, the charge recombination was suppressed and the fabricated device achieved a high PCE of 18.3%. Following this work, Serpetzoglou et al. compared the performance of $MAPbI_3$ solar cells utilizing the hydrophilic PEDOT: PSS and the non-wetting PTAA as the HTLs, respectively [150]. It was found that the non-wetting PTAA layer with a smooth surface favored the formation of uniform and larger perovskite grains. Additionally, faster relaxation times and slower bimolecular recombination rates were observed for PTAA-based devices. Owing to the merits provided by the PTAA HTL layer, the PCE of the solar cell showed remarkable enhancement from 12.6% to 15.67%.

Laser-assisted crystallization technique has also been proved to be effective to elevate the device's efficiency. For instance, Li et al. applied a laser irradiation approach to induce rapid crystallization and obtained homogeneous, pinhole-free perovskite layers [151]. Owing to the gradient distribution of laser irradiation, a proper amount of $PbI_2$ was formed on the perovskite surface, which led to self-passivation and suppressed surface states. The optimal solar cell exhibited a high PCE of 17.8%. Jeon et al. used low energy NIR laser beam to improve the crystallization and film morphology of $MAPbI_3$ perovskites [152]. The irradiation process helped with the perovskite phase transformation from a poor crystalline intermediate phase to a highly crystalline phase, contributing to devices with PCE of 11.3% and 8% on glass and flexible substrates, respectively. Konidakis et al. also demonstrated the preferable grain size and accelerated charge carrier extraction in perovskites by the laser-assisted method [153].

In 2019, the new world record PCE of 23.3% was reported by using a double-layered halide architecture (DHA) and Poly(3-hexylthiophene) (P3HT) as the HTL [154]. An ultrathin wide-bandgap halide (WBH) was introduced between the narrow-bandgap halide (NBH) and the HTL, which reduced carrier recombination at the perovskite/P3HT interface. The authors indicated that the alkyl chain in the WBH layer interacted with the P3HT and induced a self-assembled P3HT layer with suppressed trap states. Recently, further improvement in PCE was achieved and updated the world record for PCE of 25.6%. The author utilized the pseudo-halide anion formate ($HCOO^-$) to reduce the halide vacancies at the boundaries of perovskite films [27]. It was claimed that $HCOO^-$ anions passivated $I^-$ vacancies by interacting with undercoordinated $Pb^{2+}$, effectively reducing non-radiative recombination.

#### 5.1.2. Quasi-2D Lead Halide Perovskite

Despite the high efficiency of 3D LHP solar cells, their long-term stability against oxygen and moisture has largely limited the commercialization of perovskite solar cells. Quasi-2D perovskites have shown great potential to enhance device stability because their hydrophobic organic ligands can serve as an encapsulation layer [155]. In recent years, various strategies have been utilized to improve the performance of quasi-2D LHP

solar cells. In general, quasi-2D perovskite crystals tend to have random orientations where the insulating cations hinder efficient charge carrier transport through the vertical direction. As a result, quasi-2D perovskite solar cells show lower photocurrent compared to their counterparts, such as 3D and 0D perovskite solar cells [156]. Therefore, it is crucial to induce preferential vertical crystal orientation in quasi-2D perovskite. To solve this issue, Zhang et al. introduced $NH_4SCN$ as an additive in $(PEA)_2(MA)_4Pb_5I_{16}$-based solar cells [92]. The improved vertical orientation of perovskite was confirmed by the XRD results and the detailed mechanism is shown in Figure 5a. Attributed to the enhanced carrier transport through the vertical direction, the $J_{SC}$ was increased from 0.93 mA/cm$^2$ without additive to 15.01 mA/cm$^2$ with the optimal amount of additive, and the best device exhibited a high PCE of 11.01% (Figure 5b). In addition, the phase distribution of different *n* values in quasi-2D perovskite is also critical to the device's performance. Shao et al. developed a vacuum-assisted method to anneal $PEA_2MA_4Pb_5I_{16}$ perovskite [157]. On the one hand, the vacuum-assisted method resulted in a smooth and compact film with better morphology owing to its slower crystallization speed. On the other hand, this method significantly reduced the amount of $n = 2$ phases located at the bottom of the perovskite film, resulting in the promoted charge carrier transport and reduced recombination. As a result, the device by the vacuum-assisted method exhibited remarkable PCE enhancement from 3.65% to 14.14%. In 2018, the new record was achieved with a PCE of 18.2% using 3-bromobenzylammonium iodide (3BBAI)-based quasi-2D LHP [158]. In 3BBAI-based perovskite films, large *n* phases were located at the top of the film while small *n* components were at the bottom. The highly-crystalized large *n* components facilitated photon capture and carrier separation because of small bandgap and exciton binding energy whereas the vertically-orientated small *n* components were beneficial for charge transport. The device retained 82% of its original efficiency after 2400 h of storage under a relative humidity of 40% without encapsulation, demonstrating its excellent moisture stability.

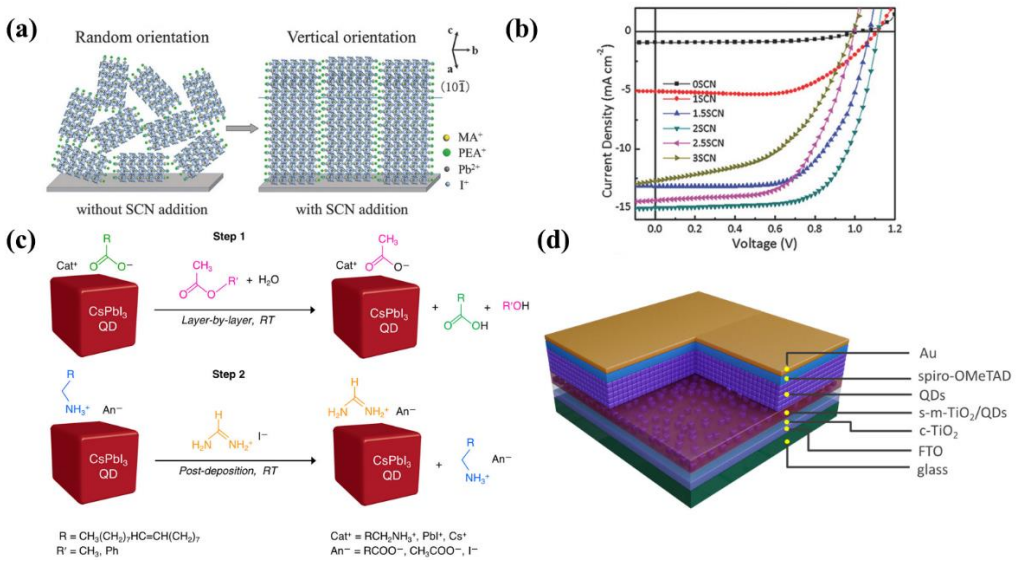


**Figure 5.** (**a**) Schematic illustration of inducing vertical crystal orientation in 2D perovskite. (**b**) The J–V curves for $(PEA)_2(MA)_4Pb_5I_{16}$-based devices with different amounts of $NH_4SCN$. (**c**) A two-step solid-state QD ligand-exchange procedure of $CsPbI_3$ PQDs. (**d**) Schematic of the PQDSC based on $CsPbI_3$ QDs and Cs-treated m-$TiO_2$ layers. (**a**,**b**) Reprinted with permission from Ref. [92]. Copyright 2018, Wiley. (**c**) Reprinted with permission from Ref. [122]. Copyright 2018, ACS. (**d**) Reprinted with permission from Ref. [159]. Copyright 2020, ACS.

### 5.1.3. 0D Lead Halide Perovskite Quantum Dots

0D PQD solar cells have also demonstrated stable device performance compared to their 3D counterparts owing to the large surface area and high surface energy of PQDs. In addition, most trap states of PQDs are located in the conduction and valence bands

attributed to the low defect formation energy. Therefore, PQDs exhibit defect-tolerant characteristics, which is favorable to optoelectronic applications [160]. However, the organic insulating ligands on the dot surface hinder effective carrier transport within the PQD film. Therefore, ligand exchange is required to substitute long-chain ligands with shorter ones in PQD solar cells. A two-step solid-state ligand-exchange method was introduced by Wheeler et al. to remove native oleate and oleylammonium ligands of $CsPbI_3$ PQDs (Figure 5c) [122]. Through the application of methyl acetate and formamidinium iodide in the first and second step, respectively, the PQD solid film showed improved charge transport and consequently, a PCE of 12% was achieved.

The engineering of charge transport layers is also critical for fabricating high-performance PQD solar cells. Chen et al. applied Cs-ion-containing methyl acetate solution to the m-$TiO_2$ electron transport layer and improved interfacial properties between m-$TiO_2$ and PQDs (Figure 5d) [159]. The $Cs^+$ ions promoted the incorporation of PQDs into the m-$TiO_2$ layer and passivated the PQD surface, resulting in an enhanced electron injection rate. Additionally, the authors utilized an ethanol-environment smoothing approach for reducing the surface roughness of the m-$TiO_2$ film. Attributed to those approaches, the optimized device exhibited a high PCE of 14.3%.

Other strategies such as site doping have also been explored. Hao et al. fabricated $Cs_{1-x}FA_xPbI_3$ PQD films with reduced defect density with the aid of OA ligands [121]. The authors demonstrated that the surface ligands were crucial for the formation of A-site vacancies and OA ligands greatly facilitated cation cross-exchange. The optimized device based on $Cs_{0.5}FA_{0.5}PbI_3$ PQDs showed an excellent PCE of 16.6% which is the highest record to date. Attributed to suppressed phase segregation in PQDs, the PQD-based devices showed superior long-term photostability compared to their 3D counterparts. The device performance of solar cells reviewed in Section 5.1 is summarized in Table 3.

**Table 3.** Summarized device performance for solar cells in Section 5.1.

| Active Materials | Voc (V) | Jsc (mA/cm$^2$) | FF (%) | PCE (%) | Ref. |
|---|---|---|---|---|---|
| $MAPbI_3$ | 0.61 | 11 | 57 | 3.81 | [26] |
| $MAPbI_3$ | 0.888 | 17.6 | 62 | 9.7 | [145] |
| $MAPbI_2Cl$ | 0.98 | 17.8 | 63 | 10.9 | [146] |
| $MAPbI_3$ | 0.992 | 17.1 | 73 | 12.9 | [147] |
| FAPbI3 | 1.06 | 24.7 | 77.5 | 20.2 | [148] |
| $MAPbI_3$ | 1.07 | 22 | 76.8 | 18.3 | [149] |
| $MAPbI_3$ | 1.01 | 20.24 | 76.67 | 15.67 | [150] |
| $MAPbI_3$ | 1.146 | 22.82 | 68 | 17.8 | [151] |
| $MAPbI_3$ | 0.91 | 14.5 | 80 | 11.3 | [152] |
| $(FAPbI_3)_{0.95}(MAPbBr_3)_{0.05}$ | 1.152 | 24.88 | 81.4 | 23.3 | [154] |
| $FAPbI_3$ | 1.189 | 26.35 | 81.7 | 25.6 | [27] |
| $(PEA)_2(MA)_4Pb_5I_{16}$ | 1.11 | 15.01 | 67 | 11.01 | [92] |
| $(PEA)_2(MA)_4Pb_5I_{16}$ | 1.1 | 17.52 | 73 | 14.14 | [157] |
| 3BBAI-based quasi-2D | 1.23 | 18.22 | 81.2 | 18.2 | [158] |
| $CsPbI_3$ QDs | 1.2 | - | - | 12 | [122] |
| $CsPbI_3$ QDs | 1.06 | 17.77 | 75.8 | 14.32 | [159] |
| $Cs_{0.5}FA_{0.5}PbI_3$ QDs | 1.17 | 18.3 | 78.3 | 16.6 | [121] |

### *5.2. Perovskite Photodetectors*

#### 5.2.1. 3D Lead Halide Perovskite

Attributed to their excellent properties, perovskites have been actively applied to photodetection technology as well. For example, a broadband photodetector with a range of 240 to 750 nm was achieved by utilizing Cs-doped $FAPbI_3$ perovskite [29]. The Cs-doping improved film quality and the favorable Schottky junction was formed between the Au and the perovskite layer (Figure 6a). As a result, the device showed a rapid response speed with a rise and fall time of 45 ns and 91 ns, respectively. In addition, highly-sensitive photodetectors were reported based on $CsPbI_xBr_{3-x}$ perovskites [161]. In the work, the

authors treated the surface of PTAA with amphiphilic PEIE to improve its wettability, leading to enhanced film coverage and quality of the above perovskite layer. The best device based on $CsPbIBr_2$ exhibited a high detectivity of $9.7 \times 10^{12}$ Jones and ultrafast response speed of 20 ns. The device remained 87% of its original photoresponsivity after more than 2000 h of storage in ambient air, which demonstrated its impressive environmental stability.

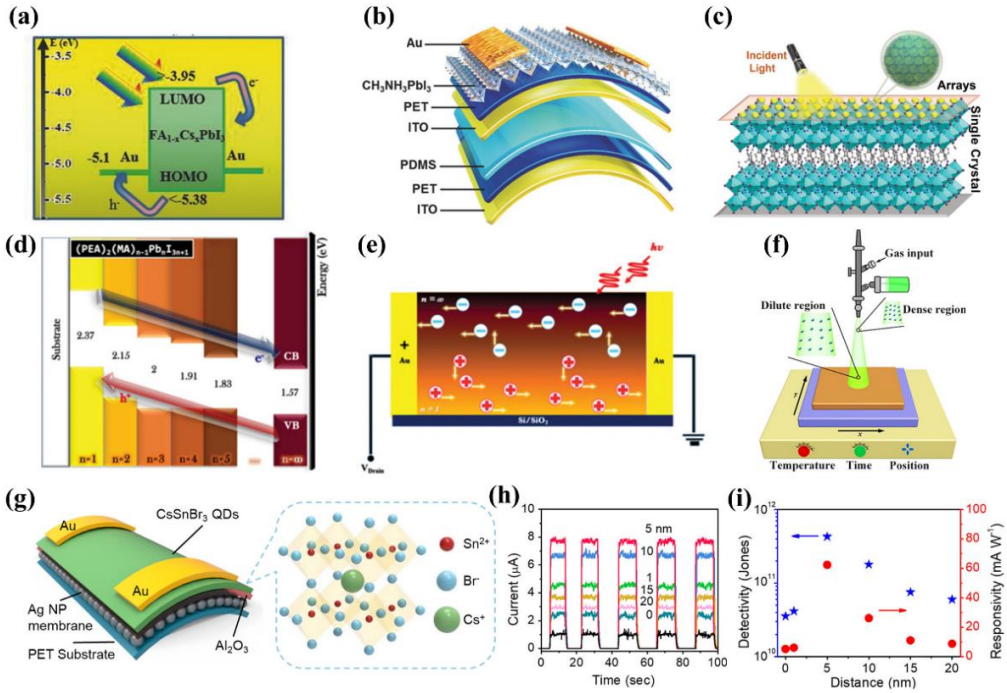


**Figure 6.** Schematic illustration of (**a**) the energy level of Cs-doped $FAPbI_3$ perovskite photodetector under incidental light, (**b**) the $MAPbI_3$-based flexible photodetector, (**c**) the array photodetector based on $(PA)_2(G)Pb_2I_7$. Schematic of (**d**) the energy band diagram and (**e**) charge transport in the gradient 2D/3D perovskite films. (**f**) Schematic illustration of the spray-coating deposition method. (**g**) Schematic of the PET/Ag NP/$Al_2O_3$/$CsSnBr_3$ QD photodetector. (**h**) Photocurrent of the photodetectors with different thicknesses of the $Al_2O_3$ layers. (**i**) The detectivity and responsivity of photodetectors with different thicknesses of the $Al_2O_3$ layers. (**a**) Reprinted with permission from Ref. [29]. Copyright 2017, WILEY. (**b**) Reprinted with permission from Ref. [162]. Copyright 2018, WILEY. (**c**) Reprinted with permission from Ref. [163]. Copyright 2019, WILEY. (**d**,**e**) Reprinted with permission from Ref. [164]. Copyright 2020, WILEY. (**f**) Reprinted with permission from Ref. [28]. Copyright 2018, ACS. (**g**–**i**) Reprinted with permission from Ref. [165]. Copyright 2021, ACS.

Furthermore, a self-powered photodetector was realized using $MAPbI_3$ as the light-harvesting layer on a flexible substrate (Figure 6b) [162]. Drop-by-drop solvent engineering of toluene was applied during spin-coating the perovskite layer to slow down the crystallization process, resulting in improved film morphology. As a result, the fabricated photodetector exhibited excellent detectivity of $1.22 \times 10^{13}$ Jones. Additionally, the flexible device was capable of harvesting omnidirectional light owing to its transparent polymer substrate. Remarkably, the device exhibited excellent physical stability even after bending 1000 times.

### 5.2.2. Quasi-2D Lead Halide Perovskite

In the case of quasi-2D LHP, a new perovskite framework employing G cation was reported for an array photodetector application (Figure 6c) which sheds light on a new branch of 2D hybrid perovskite [163]. In the work, the authors used $(PA)_2(G)Pb_2I_7$ perovskite crystals (where PA is n-pentylaminium and G is guanidinium), and achieved reduced dark current by the high-quality single crystals as well as the amplified photocurrent by the array structure. As a result, the photodetector exhibited superior performance such as

high detectivity ($6.3 \times 10^{12}$ Jones) and ultrafast response speed (3.1 ns). 2D/3D gradient $(PEA)_2(MA)_{n-1}Pb_nI_{3n+1}$ perovskite structure was employed to fabricate high-performance perovskite photodetectors [164]. As illustrated in Figure 6d, the favorable energy band alignment along the vertical heterojunctions facilitated the separation of electron-hole pairs. Additionally, carrier recirculation in the gradient perovskite films enabled a long carrier lifetime (Figure 6e). As a result, a highly sensitive photodetector was obtained with a responsivity of 149 A/W and a detectivity of $2 \times 10^{12}$ Jones.

In addition to LHP, a lead-free green photodetector was realized by integrating a 2D $(PEA)_2SnI_4$ perovskite microsheet using a ternary-solvent method [166]. Under the light illumination of 195.8 μW/cm$^2$, the device showed photoresponsivity of $3.29 \times 10^3$ A/W which is higher than its counterpart based on $(PEA)_2SnI_4$ polycrystalline film [167]. The high detectivity of $2.06 \times 10^{11}$ Jones and photoconductive gain of $8.68 \times 10^3$ was also demonstrated. This work opened up great possibilities for the high-performance photodetector for green optoelectronics.

#### 5.2.3. 0D Lead Halide Perovskite Quantum Dots

To improve the air stability of perovskite-based photodetectors, PQDs have been integrated into photodetectors. For example, Zhang et al. fabricated air-stable α-$CsPbI_3$ PQD film which exhibited high stability in material properties after exposure at a relative humidity of 30% for 60 days [168]. The authors modified the surface of α-$CsPbI_3$ QDs utilizing an up-conversion material ($NaYF_4$:Yb,Er QDs) to extend its absorption region and achieved broadband photodetection from 260 nm to 1100 nm. Additionally, a high on/off ratio of $10^4$, a responsivity of 1.5 A/W, and a short response time (less than 5ms) were also demonstrated. In spite of their high air stability, the yield of PQDs is relatively low compared to their 3D and quasi-2D counterparts. Furthermore, a large volume of materials is wasted during a conventional spin-coating method, limiting the scalability of PQD-based photodetectors. To resolve this issue, a spray-coating approach was developed to deposit the $CsPbBr_3$ QD layer in a photodiode (Figure 6f) [28]. This spray technique enabled a high material utilization rate of 32% compared to that of the spin-coating method (only 1%). Additionally, the authors precisely adjusted the substrate temperature and spray time to obtain the crack-free PQD film and demonstrated a large-area photodiode of $10 \times 10$ cm$^2$ with a high detectivity of $1 \times 10^{14}$ Jones.

In addition to LHP-based PQDs, lead-free PQDs have also been actively researched to realize an environmentally-friendly photodetector. Ma et al. synthesized lead-free $CsSnBr_3$ QDs and introduced a plasmonic/dielectric nanostructure to optimize the performance of a flexible photodetector (Figure 6g) [165]. Plasmonic Ag nanoparticles (NPs) were applied to improve the light absorption capability of the $CsSnBr_3$ PQDs through localized surface plasmon resonance. A dielectric $Al_2O_3$ spacer layer was inserted between the PQD layer and the Ag membrane to reduce the surface energy quenching. As shown in Figure 6h, with the optimized thickness of the $Al_2O_3$ layer, the photocurrent showed a remarkable enhancement which was 7.5 times higher than that of the device without the dielectric layer. The self-assembled Ag NPs membrane could release some bending tension, which enabled the flexible device with good mechanical durability. The photodetector showed the maximum detectivity of $4.27 \times 10^{11}$ Jones and responsivity of 62.3 mA/W (Figure 6i), which are among the highest values for Sn-based perovskite photodetectors.

Perovskites have great potential for future generation optoelectronic applications due to their fascinating material properties. Nevertheless, some prominent issues regarding the device structures and inherent material defects hampered their further development towards commercialization. First, there is an urgent need for replacing the commonly used carrier transport materials. On the one hand, most perovskite optoelectronic devices utilized PEDOT: PSS as the hole transport layer, whose acidity and hygroscopicity would severely deteriorate the device's durability [169]. On the other hand, as the popular electron transport material, $TiO_2$ suffered from a high density of trap states and the required high-temperature sintering (400–500 °C) process [170]. In addition, the devices generally showed

poor stability and large recombination loss due to the sensitivity and a great number of defects of perovskites. The introduction of passivation and encapsulation layers is expected to solve these problems. The device performance of photodetectors reviewed in Section 5.2 is summarized in Table 4.

**Table 4.** Summarized device performance of photodetectors in Section 5.2.

| Active Materials | Response Range (nm) | R (A/W) | D* (Jones) | $\tau_{rise}/\tau_{fall}$ | Ref. |
|---|---|---|---|---|---|
| $FA_{0.85}Cs_{0.15}PbI_3$ | 240–750 | 5.7 | $2.7 \times 10^{13}$ | 45 ns/91 ns | [29] |
| $CsPbIBr_2$ | 400–580 | 0.28 | $9.7 \times 10^{12}$ | 20 ns/20ns | [161] |
| $MAPbI_3$ | - | 0.418 | $1.22 \times 10^{13}$ | - | [162] |
| $(PA)_2(G)Pb_2I_7$ | 420–700 | ~47 | $6.3 \times 10^{12}$ | 0.94 ns/2.18 ns | [163] |
| $(PEA)_2(MA)_{n-1}Pb_nI_{3n+1}$ | 420–760 | 149 | $2 \times 10^{12}$ | 69 ms/103 ms | [164] |
| $(PEA)_2SnI_4$ | - | $3.29 \times 10^3$ | $2.06 \times 10^{11}$ | 0.37 s/3.05 s | [166] |
| $CsPbI_3$ QDs | 260–1100 | 1.5 | - | <5 ms/<5 ms | [168] |
| $CsPbBr_3$ QDs | - | 3 | $10^{14}$ | | [28] |
| $CsSnBr_3$ QDs | 300–630 | 0.0623 | $4.27 \times 10^{11}$ | 50 ms/51 ms | [165] |

## 6. 2D Materials/Perovskites Interface Engineering

As we discussed above, 2D materials and perovskites have achieved great success during the past decade in the field of optoelectronics. However, challenges still remain and there is high demand for further improving the performance of the devices. For instance, the performance of 2D materials-based optoelectronics is generally limited by weak light absorption caused by their atomic-scale thicknesses, whereas perovskites-based devices suffer from severe stability issues against oxygen and moisture [33]. In recent years, the concept of 2D material/perovskite heterostructure has been proposed. Devices based on this novel structure exhibited improved performance and stability by taking advantage of the outstanding optical properties of perovskites and the fascinating electrical and optical properties of 2D materials in addition to an encapsulation effect. Furthermore, there are large families of 2D materials and perovskites, opening up great possibilities for engineering the heterostructures [33]. In this part, we summarize recent achievements in solar cells and photodetectors based on 2D material/perovskite heterostructure.

### *6.1. 2D Material/Perovskite Heterostructure for Solar Cells*

2D materials have excellent material properties, such as low trap density and high carrier mobility. Therefore, they have been considered promising candidates for charge transport layers in perovskite solar cells [171].

#### 6.1.1. Graphene Derivative/Perovskite Heterostructure

Derivatives of graphene have been widely utilized in perovskite solar cells to improve device performance and stability. For example, graphene oxide (GO) was introduced as a hole transport layer (HTL) in $MAPbI_{3-x}Cl_x$-based solar cells by Wang et al. [172]. The pristine GO was treated with ammonia, which helped with improved film coverage and crystallinity of the perovskite layer. It was reported that the better wettability of ammonia-treated GO to DMF precursors, as well as the strong Pb–N coordination bond between perovskites and a-GO, enhanced the crystallization, yielding a PCE of 14.14%. However, the application of GO in high-performance perovskite solar cells is largely restricted because of its insulating characteristics and a high degree of surface oxygen [173]. To solve this issue, rGO was employed as the HTL layer to the perovskite solar cell application as the rGO has low surface oxygen content and an intrinsic passivation effect towards water and oxygen [174]. Jokar et al. demonstrated that the reduction of oxygen atoms decreased charge recombination caused by the localized holes at the rGO/perovskite interface, contributing to the elevated PCE of 16.4% [175]. Similarly, Chen et al. substituted acid and hydrophilic PEDOT: PSS with covalently sulfated graphene oxide (oxo-G1) and employed it as the HTL layer [169]. Oxo-G1 reduced the speed of water ingress into the device and

improved its stability in ambient air. As a result, the rGO/$MAPbI_3$ heterostructure device demonstrated enhanced PCE and much slower degradation over time compared to devices with PEDOT: PSS as HTL. Another approach was introduced by Agresti et al. The authors inserted lithium neutralized graphene oxide (GO-Li) as the electron transport layer (ETL) in $MAPbI_3$ perovskite solar cells (Figure 7b) [176]. The GO-Li formed a favorable band alignment with titanium dioxide ($TiO_2$), which significantly facilitated electron extraction from the perovskite to the mesoporous $TiO_2$ (m-$TiO_2$) layer. Compared to the reference sample without GO-Li, the fabricated device showed increased $J_{sc}$ (+10.5%) and FF (+7.5%) as well as reduced hysteresis. Additionally, GO-Li passivated oxygen vacancies of m-$TiO_2$, resulting in enhanced stability under illumination.

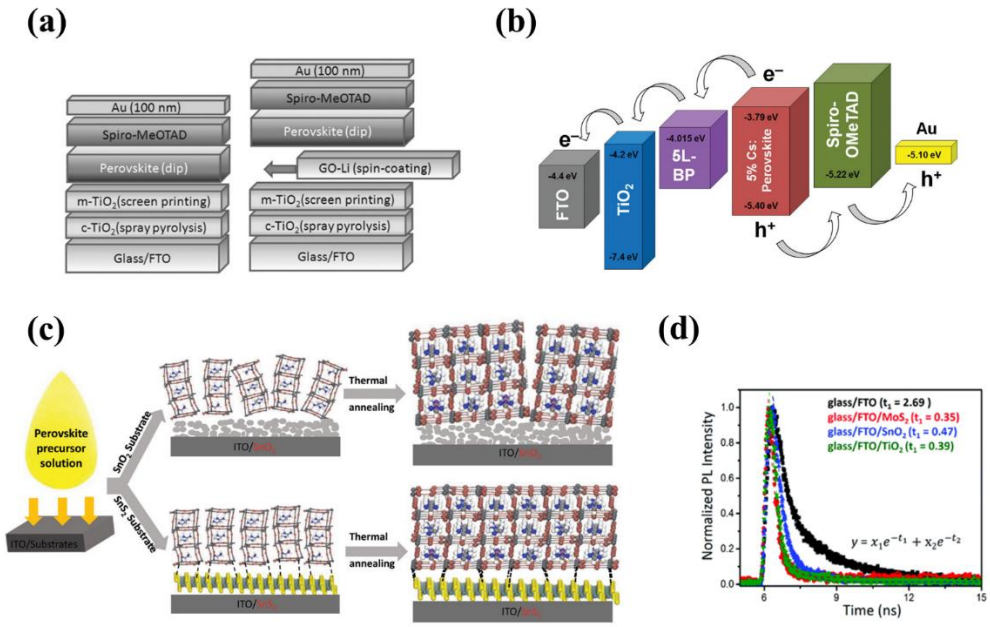


**Figure 7.** (**a**) Schematic structure of the reference device and GO-Li device. (**b**) Schematic illustration of energy diagram and carrier transfer in the perovskite solar cell. (**c**) The schematic illustration of the formation of perovskite films on $SnO_2$ and $SnS_2$ ETLs. (**d**) The TRPL results of perovskite films with different ETLs. (**a**) Reprinted with permission from Ref. [176]. Copyright 2016, WILEY. (**b**) Reprinted with permission from Ref. [177]. Copyright 2019, WILEY. (**c**) Reprinted with permission from Ref. [178]. Copyright 2018, WILEY. (**d**) Reprinted with permission from Ref. [170]. Copyright 2019, RSC.

### 6.1.2. TMDC/Perovskite Heterostructure

Similar to the derivatives of graphene layers, TMDC has been widely employed as a charge transport and/or passivation layer as well. Singh et al. synthesized an $MoS_2$ layer by a facile microwave-assisted method as an ETL in $MAPbI_3$ perovskite solar cells for the first time [170]. As the $MoS_2$ has high electron mobility and a low density of trap states, a perovskite film with the $MoS_2$ layer exhibited reduced nonradiative recombination compared to the perovskite solar cell with $TiO_2$. Particularly, as the TRPL results show in Figure 7c, the perovskite film with the $MoS_2$ layer as a quencher showed the shortest recombination lifetime, indicating the efficient charge transfer of the $MAPbI_3$/$MoS_2$ heterostructure. The as-obtained solar cell exhibited a PCE of 13.14%, which was comparable to that of $TiO_2$- and $SnO_2$-based devices. Similarly, an $SnS_2$ layer was employed as the ETL for the $FA_{0.75}MA_{0.15}Cs_{0.1}PbI_{2.65}Br_{0.35}$ perovskite solar cell where the $SnS_2$ layer was prepared by a self-assembled stacking deposition method [178]. The $SnS_2$ nanosheet induced heterogeneous nucleation of the perovskite and enabled uniform film with homogeneous grain size. The interaction between Pb and S atoms at the $SnS_2$/perovskite interface effectively passivated defect states and improved charge extraction (Figure 7d). The fabricated

device showed a higher PCE of 20.12% in comparison with the conventional $SnO_2$-based device (17.72%).

The TMDC/perovskite heterostructure was also widely applied to the HTL. For example, Kim et al. fabricated $MAPbI_{3-x}Cl_x$ solar cells utilizing $MoS_2$ and $WS_2$ as the HTL [179]. Attributed to the suitable work functions that $MoS_2$ and $WS_2$ have, the $MoS_2$- and $WS_2$-based perovskite solar cells exhibited a PCE of 9.53% and 8.02%, which are comparable to PEDOT: PSS-based devices (9.93%). Similarly, $MoSe_2$ was employed as HTL to form the $MoSe_2/MAPbI_3$ heterostructure in the perovskite solar cell, and a PCE of 8.23% was attained [180]. The authors discovered that increasing the annealing temperature of $MoSe_2$ from 500, 600 to 700 °C had a positive effect on the perovskite crystallization, resulting in improved device performance.

#### 6.1.3. Other 2D Material/Perovskite Heterostructure

Finally, other 2D materials have also been widely employed in perovskite solar cells. A phosphorene, an isolated single layer of BP, is one of the promising candidates for the heterostructure because it has a high carrier mobility of over 1000 $cm^2\ V^{-1}\ s^{-1}$ and formed good energy band alignment in the device structure [177]. By using a simple vortex fluidic mediated exfoliation method, the phosphorene nanosheet was attained and applied to the perovskite solar cell as an ETL (Figure 7e). The phosphorene nanosheet effectively promoted electron transfer, and therefore the average PCE of the devices improved from 14.32% to 16.53%. Recently, a $Ti_3C_2T_x$ MXene nanosheet was also employed as the ETL in $MAPbI_3$-based perovskite solar cells [181]. In the work, the authors revealed that the UV-ozone treatment of $Ti_3C_2T_x$ induced oxide-like Ti–O bonds, resulting in enhanced electron transfer and suppressed nonradiative recombination at the $Ti_3C_2T_x/MAPbI_3$ interface. Attributed to this, the device showed improved performance with PCE significantly increased from 5% to 17.17%. The device performance of solar cells reviewed in Section 6.1 is summarized in Table 5.

**Table 5.** Summarized device performance for solar cells in Section 6.1.

| Heterostructure | Voc (V) | Jsc ($mA/cm^2$) | FF (%) | PCE (%) | Ref. |
|---|---|---|---|---|---|
| $GO/MAPbI_{3-x}Cl_x$ | 1 | 18.4 | 76.8 | 14.14 | [172] |
| $rGO/MAPbI_3$ | 0.962 | 22.1 | 77 | 16.4 | [175] |
| $rGO/MAPbI_3$ | 1.08 | 18.06 | 77.7 | 15.2 | [169] |
| $GO/MAPbI_3$ | 0.859 | 19.61 | 70.3 | 11.8 | [176] |
| $MoS_2/MAPbI_3$ | 0.89 | 21.7 | 63.8 | 13.14 | [170] |
| $SnS_2/FA_{0.75}MA_{0.15}Cs_{0.1}PbI_{2.65}Br_{0.35}$ | 1.161 | 23.55 | 73 | 20.12 | [178] |
| $MoS_2/MAPbI_{3-x}Cl_x$ | 0.96 | 14.89 | 67 | 9.53 | [179] |
| $WS_2/MAPbI_{3-x}Cl_x$ | 0.82 | 15.91 | 64 | 8.02 | [179] |
| $MoSe_2/MAPbI_3$ | 1.02 | 14.45 | 55.8 | 8.23 | [180] |
| $BP/(FAPbI_3)_x(MAPbBr_3)_{1-x}$ | 1.08 | 23.32 | 0.71 | 17.85 | [177] |
| $Ti_3C_2T_x$ MXene/$MAPbI_3$ | 1.08 | 22.63 | 70 | 17.17 | [181] |

### *6.2. 2D material/Perovskite Heterostructure for Photodetectors*

#### 6.2.1. Graphene/Perovskite Heterostructure

Graphene has attracted much research interest in the field of photodetection owing to its high charge carrier mobility and broad absorption band. However, the development of graphene-based photodetectors has been largely restricted due to the rapid recombination rate and weak light absorption in pristine graphene. Various approaches have been applied to solve these problems, including coupling graphene with silicon waveguide [133] or microcavity [182], and hybridizing graphene with lead sulfide QDs [183]. However, some of these strategies require complicated fabrication procedures, or the obtained devices only have limited operating bandwidth and photosensitivity. To further improve the device performance, researchers integrated newly-emerged perovskite materials with graphene and great progress has been made in the past few years.

For 3D $MAPbI_3$ perovskite, the heterostructure with graphene demonstrated a high device performance [184]. Due to the formation of the heterostructure, electrons in the graphene layer are transported to the perovskite layer. These electrons filled the empty states caused by light absorption in the valence band, effectively reducing the probability of carrier recombination within the perovskite layer. Attributed to this photogating effect, the photodetector exhibited high photoresponsivity of 180 A/W, EQE of $5 \times 10^4$%, and detectivity $\approx 10^9$ Jones at light illumination power of 1 μW.

Recently, single-crystal $MAPbBr_3$ with the graphene heterostructure has also been demonstrated as shown in Figure 8a [185]. Enhanced charge transport and consequently high photocurrent were achieved in the device, which was attributed to low defect density in the single crystal perovskite and improved charge carrier separation by the internal electric field as shown in Figure 8b. Compared to devices based on pure graphene, the photoresponse of the graphene/$MAPbI_3$ heterostructure photodetector was enhanced by an order, with high responsivity (1017.1 A/W), detectivity ($2.02 \times 10^{13}$ Jones), and photoconductive gain ($2.37 \times 10^3$).

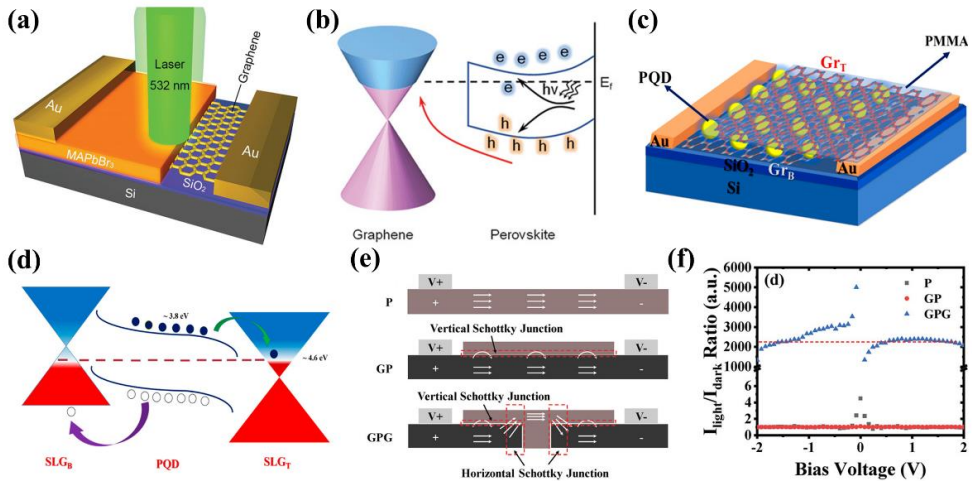


**Figure 8.** (**a**) Schematic of the graphene/$MAPbI_3$ single crystal photodetector. (**b**) Energy band diagram of the graphene/$MAPbI_3$ single crystal heterostructure. (**c**) Schematic of the graphene/PQDs/graphene phototransistor. (**d**) Energy band diagram of the graphene/PQDs/graphene heterostructure. (**e**) Schematic illustration of devices based on perovskite layer (P), graphene/perovskite (GP), and graphene/perovskite/graphene (GPG) structure. (**f**) The $I_{light}/I_{dark}$ ratio under different bias voltages. (**a**,**b**) Reprinted with permission from Ref. [185]. Copyright 2020, WILEY. (**c**,**d**) Reprinted with permission from Ref. [186]. Copyright 2019, ACS. (**e**,**f**) Reprinted with permission from Ref. [187]. Copyright 2019, WILEY.

In addition, graphene/perovskite/graphene (GPG) heterostructure was widely used for the photodetector application. For example, Bera et al. reported a broadband phototransistor based on the graphene/$MAPbBr_3$ PQDs/graphene heterostructure as shown in Figure 8c [186]. Due to the asymmetric potential at the interfaces (Figure 8d), electrons were transferred to the top graphene layer while holes were driven towards the bottom graphene layer under light illumination. The Schottky barrier suppressed carrier recombination and enhanced the photocurrent. In addition, the PMMA layer on the top of the device reduced the reflectivity of the incident light as well as served as an encapsulation layer against ambient air. The device exhibited high photoresponsivity of ~$10^9$ A/W, a fast response time of ~20 μs, and stable photodetection for over six months. Similarly, a photodetector consisting of the graphene/$MAPbI_3$/graphene structure was reported by Chen et al. in 2019 [187]. As shown in Figure 8e, in the GPG device, a perovskite channel was introduced in the bottom graphene layer, thus creating vertical and horizontal Schottky junctions for effective carrier transport. Compared to devices with other structures, the GPG device had the highest $I_{light}/I_{dark}$ ratio because the dark current was reduced by the perovskite channel with large resistance (Figure 8f).

The GPG phototransistor showed a high on/off switch ratio of $2.6 \times 10^3$ and detectivity of $3.55 \times 10^9$ Jones. The authors also fabricated the GPG structure on PET substrates and the obtained flexible device exhibited excellent reliability and bendability.

#### 6.2.2. TMDC/Perovskite Heterostructure

A variety of TMDC/perovskite heterostructures have been employed for photodetector applications. For example, Lu et al. developed a high-performance phototransistor by integrating a $WSe_2$ monolayer and $MAPbI_3$ perovskite layer [188]. The authors used a focused laser beam to passivate the chalcogen vacancies in the pristine $WSe_2$ film and significantly improved its conductivity. The combination of perovskite with high absorption coefficient and defect-free $WSe_2$ resulted in excellent device performance which is three orders of magnitude higher than that of a pristine $WSe_2$ device.

Similarly, hybrid photodetectors comprising of $MoS_2/MAPbI_3$ heterostructure were proposed by employing different phases of $MoS_2$ layers, namely 1T and 2H [189]. The authors compared the performance of the metallic 1T phase and the semiconducting 2H phase of $MoS_2$ in photodetectors. On the one hand, the 1T phase is capable of accommodating the injection of more carriers owing to its metallic characteristic, resulting in enhanced photocurrent. On the other hand, the photogenerated carriers injected into $MoS_2$ have a high probability of recombination in the 1T-$MoS_2/MAPbI_3$ device (Figure 9a), which leads to a high dark current. As a result, the 1T-$MoS_2/MAPbI_3$ device exhibited high photoresponsivity with a low on/off ratio while the 2H-$MoS_2/MAPbI_3$ device had reasonable photoresponse with an increased on/off ratio.

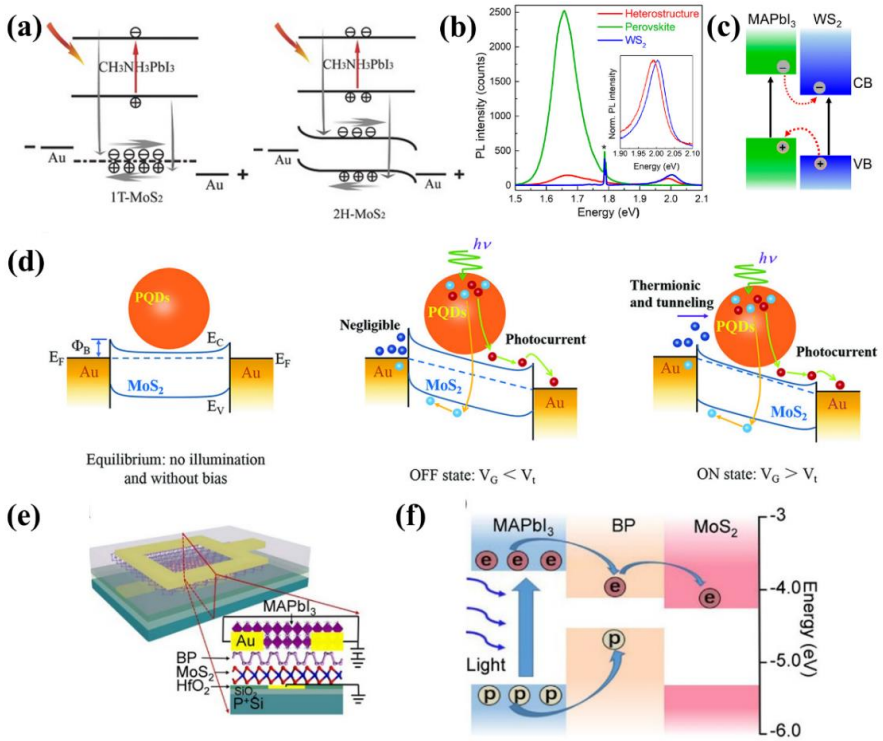


**Figure 9.** (**a**) Charge transfer mechanism of 1T-$MoS_2/MAPbI_3$ and 2H-$MoS_2/MAPbI_3$ photodetectors. (**b**) PL spectra of the fabricated heterostructure, isolated perovskite, and $WS_2$. (**c**) Schematic illustration of type II band alignment and charge transfer at the $MAPbI_3/WS_2$ heterostructure. (**d**) Schematic of charge transfer for the PQDs/$MoS_2$ device. Schematic illustration of the (**e**) perovskite/BP/$MoS_2$ photodiode and (**f**) charge transfer in the heterostructure. (**a**) Reprinted with permission from Ref. [189]. Copyright 2016, WILEY. (**b**,**c**) Reprinted with permission from Ref. [190]. Copyright 2019, ACS. (**d**) Reprinted with permission from Ref. [191]. Copyright 2018, WILEY. (**e**,**f**) Reprinted with permission from Ref. [192]. Copyright 2019, ACS.

In 2019, Erkõlõc et al. demonstrated photodetectors based on ultrathin $MAPbI_3/WS_2$ heterostructures by a vapor-phase growth approach [190]. $PbI_2$ was deposited onto monolayer $WS_2$, followed by the successive conversion to $MAPbI_3$ through MAI intercalation. $WS_2$ served as an effective template for the site-selective growth of ultrathin perovskite film at a large scale, avoiding any damage to the perovskite that would be caused by post-growth lithography processes. The strong PL quenching indicated effective charge transfer between $MAPbI_3$ and $WS_2$ layers due to type II band alignment (Figure 9b,c). Attributed to the strong light absorption capability of the perovskite layer, the fabricated photodetector showed enhanced responsivity of 43.6 A/W compared to the $WS_2$-only device of 3.3 A/W.

In addition to 3D perovskites, quasi-2D and PQDs have also been applied in heterostructures. For example, Fu et al. hybridized $MoS_2$ with quasi-2D $(BA)_2(MA)_2Pb_3I_{10}$ perovskite for sensitive photodetection [144]. Due to the facile charge separation at the $MoS_2$/perovskite interface, the hybrid photodetector exhibited excellent performance with two and six orders of magnitude improvement for detectivity ($4 \times 10^{10}$ Jones) and photoresponsivity ($10^4$ A/W). For PQDs, an ultrasensitive photodetector was demonstrated using the hybrid structure of $CsPbI_{3-x}Br_x$ QDs and monolayer $MoS_2$ [191]. Attributed to favorable energy band alignment at the PQDs/$MoS_2$ interface, the photocurrent of the hybrid device was improved by 15.3 times compared to that of the $MoS_2$-only device. As illustrated in Figure 9d, the Schottky barrier determined by the applied gate voltage and the photogating effect together modulated the dark current and photoresponsivity in the device. As a result, the optimized photodetector displayed high photoresponsivity of $7.7 \times 10^4$ A/W, detectivity of $5.6 \times 10^{11}$ Jones and EQE of over $10^7$%.

#### 6.2.3. Other 2D Materials/Perovskite Heterostructure

Other 2D materials, such as BP and nitrides (MXenes), have also shown great potential for integrating with perovskites. For instance, Muduli et al. integrated $CsPbBr_3$ PQDs on the surface of few-layer BP (FLBP) [193]. Due to charge transfer between the $CsPbBr_3$ PQD and FLBP layers, the $CsPbBr_3$ PQD-FLBP device showed significant photoresponse in comparison with the $CsPbBr_3$ PQD-only device with negligible photocurrent. Following this work, a hybrid photodiode was proposed which consisted of the perovskite/BP/$MoS_2$ double heterostructures (Figure 9e) [192]. As illustrated in Figure 9f, type I and type II band alignments are formed at the perovskite/BP and BP/$MoS_2$ heterointerface, respectively. Under light illumination, photogenerated carriers in the perovskite layer diffused into the BP layer, followed by efficient carrier separation by the built-in electric field at the interface of BP and $MoS_2$. As a result, the photodiode exhibited high detectivity of $1.3 \times 10^{12}$ Jones as well as a fast response of 150/240 µs.

For flexible photodetectors, a large-area photodetector was realized by utilizing a 2D $CsPbBr_3$ nanosheet as the light-absorbing material and MXene as electrodes, which was fabricated by all-sprayed-processable methods [194]. The obtained device showed a superior on/off ratio of $2.3 \times 10^3$ and a fast response speed of 18 ms, which was attributed to the highly conductive MXene electrodes, and excellent crystallinity of $CsPbBr_3$ nanosheet, and well-matched energy level at the $CsPbBr_3$/MXene interface. In addition, the device retained 85% of its original photocurrent after applying 1500 times of cyclic bending, demonstrating its excellent physical stability. The device performance of photodetectors reviewed in Section 6.2 is summarized in Table 6.

**Table 6.** Summarized device performance of photodetectors in Section 6.2.

| Materials | Response Range | R (A/W) | D* (Jones) | $\tau_{rise}/\tau_{fall}$ | Ref. |
|---|---|---|---|---|---|
| Graphene/$MAPbI_3$ | UV–Visible | 180 | ~$10^9$ | 87 ms/540 ms | [184] |
| Graphene/$MAPbI_3$ | - | 1017.1 | $2.02 \times 10^{13}$ | 50.9 ms/26 ms | [185] |
| Graphene/$MAPbBr_3$ QDs | UV-IR | ~$3 \times 10^9$ | $8.7 \times 10^{15}$ | <50 µs/<50 µs | [186] |
| Graphene/$MAPbI_3$ | 650–900 nm | 0.022 | $3.55 \times 10^9$ | - | [187] |
| $WSe_2$/$MAPbI_3$ | - | 110 | $2.2 \times 10^{11}$ | - | [188] |
| $MoS_2$/$MAPbI_3$ | UV–Visible | 3096 | $7 \times 10^{11}$ | 0.45 s/0.75 s | [189] |
| $WS_2$/$MAPbI_3$ | - | 43.6 | - | | [190] |
| $MoS_2$/$(BA)_2(MA)_2Pb_3I_{10}$ | - | $10^4$ | $4 \times 10^{10}$ | - | [144] |
| $MoS_2$/$CsPbI_{3-x}Br_x$ | UV–Visible | $7.7 \times 10^4$ | $5.6 \times 10^{11}$ | 0.59 s/0.32 s | [191] |
| BP/$CsPbBr_3$ QDs | - | - | $1.3 \times 10^{12}$ | 150 µs/240 µs | [193] |
| MXene/$CsPbBr_3$ | - | 0.0449 | $6.4 \times 10^8$ | 48 ms/18 ms | [194] |

## 7. Perspectives

To date, the 2D material/perovskite heterostructure has demonstrated great potential for advanced optoelectronics and numerous efforts have been made to improve the performance of devices. However, several challenges still remain which hinder the further improvement of commercial applications.

An open challenge is that the heterostructure generally suffers from poor stability in the ambient air because perovskite is very sensitive to humidity, heat, and light. In recent years, novel perovskites have been developed and demonstrated to be more stable than 3D perovskites. 2D RP perovskites have attracted much attention because their hydrophobic organic ligands could protect perovskites from water invasion [195]. In addition, it was reported that ion migration was suppressed in RP perovskites, which would alleviate the degradation process of perovskite [196]. Similarly, 2D DJ perovskites have emerged as a potential material with excellent environmental stability. Compared to RP perovskites, the adjacent inorganic layers of DJ perovskites were bridged by diammonium ligands which eliminate the vdWs gap and shorten the inter-slab distance, resulting in improved stability [197]. In addition, researchers have proposed a series of encapsulation materials for perovskite-based devices. For instance, Li et al. encapsulated $CsPbBr_3$ nanocrystals into dense $SiO_2$ solid and the PL intensity of perovskite maintained 100% of its initial value for 1000 h under illumination [198].

Apart from the stability issue, the large-scale production of 2D material/perovskite heterostructures has been limited by fabrication methods. On the one hand, the majority of high-quality heterostructures are constructed using solid-state methods, such as wet/dry transfer, mechanical exfoliation, CVD, and physical vapor deposition (PVD), which require complicated procedures and high cost. On the other hand, although facile solution-processed methods provide access to large yield, the heterostructures suffer from low quality and reduced charge transport due to the poor contact at the interface [33]. In this regard, epitaxial growth might be a promising strategy to solve this dilemma. It was demonstrated that this approach enabled precise control over the crystal phases, exposed interfaces, size, and morphology of the hybrid nanostructures with relatively low cost [199].

Lastly, the most widely researched perovskites in the heterostructures involve toxic and hazardous heavy metals, particularly Pb, which is harmful to the environment as well as human beings. Considerable efforts have been made toward replacing Pb with environmentally friendly or less hazardous elements, such as Sn, Mn, and Zn, where Sn is the most promising candidate among those substitutes [200–202]. However, Sn-based devices showed inferior performance in comparison with their lead counterparts because of the high density of defects in perovskite lattice, and severe oxidation of Sn from +2 to +4 states restricted their long-term stability. Therefore, the development of perovskites based on non-toxic substances is of high importance for future advanced optoelectronics.

## 8. Conclusions

The review covered the synthesis methods of 2D materials and perovskites, as well as their applications in solar cells and photodetectors. First, the basic properties and common synthesis routes of 2D materials and perovskites were addressed to provide a fundamental picture of these materials. Then, we summarized the recent research progress of optoelectronic devices based on 2D materials or perovskites. Despite their great potential in state-of-the-art optoelectronics, some issues regarding weak light absorption and poor stability restricted their commercial applications, which led to the introduction of 2D material/perovskite heterostructure. We analyzed the underlying benefits of this novel concept and reviewed the recent development of optoelectronic devices applying this heterostructure. Finally, we introduced the existing challenges and possible solutions for developing stable and high-quality 2D material/perovskite heterostructures, and also the need for environmentally friendly perovskites for green optoelectronics.

**Author Contributions:** S.M. and T.L. contributed equally to this work. T.L., Y.L., X.Z. and Y.X. did literature reviews for the materials section. S.M., Y.D., J.G. and F.S. did literature reviews for device parts. S.M. and T.L. wrote the manuscript under the supervision of Y.C. All authors have read and agreed to the published version of the manuscript.

**Funding:** This research received no external funding.

**Data Availability Statement:** Not applicable.

**Acknowledgments:** Y.C. thank UM-SJTU Joint Institute for its support of the work.

**Conflicts of Interest:** The authors declare no conflict of interest.

## References

1. Ali, N.; Shehzad, N.; Uddin, S.; Ahmed, R.; Jabeen, M.; Kalam, A.; Al-Sehemi, A.G.; Alrobei, H.; Kanoun, M.B.; Khesro, A.; et al. A Review on Perovskite Materials with Solar Cell Prospective. *Int. J. Energy Res.* **2021**, *45*, 19729–19745. [CrossRef]
2. Li, L.; Ye, S.; Qu, J.; Zhou, F.; Song, J.; Shen, G. Recent Advances in Perovskite Photodetectors for Image Sensing. *Small* **2021**, *17*, 2005606. [CrossRef] [PubMed]
3. Liu, S.; Zhang, X.; Gu, X.; Ming, D. Photodetectors Based on Two Dimensional Materials for Biomedical Application. *Biosens. Bioelectron.* **2019**, *143*, 111617. [CrossRef] [PubMed]
4. Zhao, Z.; Liu, J.; Liu, Y.; Zhu, N. High-Speed Photodetectors in Optical Communication System. *J. Semicond.* **2017**, *38*, 121001. [CrossRef]
5. Mahapatra, A.; Prochowicz, D.; Tavakoli, M.M.; Trivedi, S.; Kumar, P.; Yadav, P. A Review of Aspects of Additive Engineering in Perovskite Solar Cells. *J. Mater. Chem. A* **2020**, *8*, 27–54. [CrossRef]
6. Ghosh, S.; Mishra, S.; Singh, T. Antisolvents in Perovskite Solar Cells: Importance, Issues, and Alternatives. *Adv. Mater. Interfaces* **2020**, *7*, 2000950. [CrossRef]
7. Li, X.; Hoffman, J.M.; Kanatzidis, M.G. The 2D Halide Perovskite Rulebook: How the Spacer Influences Everything from the Structure to Optoelectronic Device Efficiency. *Chem. Rev.* **2021**, *121*, 2230–2291. [CrossRef]
8. Zhang, F.; Lu, H.; Tong, J.; Berry, J.J.; Beard, M.C.; Zhu, K. Advances in Two-Dimensional Organic–Inorganic Hybrid Perovskites. *Energy Environ. Sci.* **2020**, *13*, 1154–1186. [CrossRef]
9. Chen, J.; Jia, D.; Johansson, E.M.J.; Hagfeldt, A.; Zhang, X. Emerging Perovskite Quantum Dot Solar Cells: Feasible Approaches to Boost Performance. *Energy Environ. Sci.* **2021**, *14*, 224–261. [CrossRef]
10. Kolobov, A.V.; Tominaga, J. *Two-Dimensional Transition-Metal Dichalcogenides*; Springer Series in Materials Science; Springer International Publishing: Cham, Switzerland, 2016; Volume 239, ISBN 978-3-319-31449-5.
11. Shi, Y.; Li, H.; Li, L.-J. Recent Advances in Controlled Synthesis of Two-Dimensional Transition Metal Dichalcogenides via Vapour Deposition Techniques. *Chem. Soc. Rev.* **2015**, *44*, 2744–2756. [CrossRef]
12. Whitener, K.E.; Sheehan, P.E. Graphene Synthesis. *Diam. Relat. Mater.* **2014**, *46*, 25–34. [CrossRef]
13. Chen, S.; Shi, G. Two-Dimensional Materials for Halide Perovskite-Based Optoelectronic Devices. *Adv. Mater.* **2017**, *29*, 1605448. [CrossRef] [PubMed]
14. Raja, S.N.; Bekenstein, Y.; Koc, M.A.; Fischer, S.; Zhang, D.; Lin, L.; Ritchie, R.O.; Yang, P.; Alivisatos, A.P. Encapsulation of Perovskite Nanocrystals into Macroscale Polymer Matrices: Enhanced Stability and Polarization. *ACS Appl. Mater. Interfaces* **2016**, *8*, 35523–35533. [CrossRef] [PubMed]
15. Konidakis, I.; Karagiannaki, A.; Stratakis, E. Advanced Composite Glasses with Metallic, Perovskite, and Two-Dimensional Nanocrystals for Optoelectronic and Photonic Applications. *Nanoscale* **2022**, *14*, 2966–2989. [CrossRef] [PubMed]

16. Lee, C.; Wei, X.; Kysar, J.; Hone, J. Measurement of the Elastic Properties and Intrinsic Strength of Monolayer Graphene. *Science* **2008**, *321*, 382–385. [CrossRef] [PubMed]
17. Balandin, A.A.; Ghosh, S.; Bao, W.; Calizo, I.; Teweldebrhan, D.; Miao, F.; Lau, C.N. Superior Thermal Conductivity of Single-Layer Graphene. *Nano Lett.* **2008**, *8*, 902–907. [CrossRef]
18. Xu, Y.; Shi, Z.; Shi, X.; Zhang, K.; Zhang, H. Recent Progress in Black Phosphorus and Black-Phosphorus-Analogue Materials: Properties, Synthesis and Applications. *Nanoscale* **2019**, *11*, 14491–14527. [CrossRef]
19. Ma, X.; Wu, X.; Wang, H.; Wang, Y. A Janus MoSSe Monolayer: A Potential Wide Solar-Spectrum Water-Splitting Photocatalyst with a Low Carrier Recombination Rate. *J. Mater. Chem. A* **2018**, *6*, 2295–2301. [CrossRef]
20. Eda, G.; Yamaguchi, H.; Voiry, D.; Fujita, T.; Chen, M.; Chhowalla, M. Photoluminescence from Chemically Exfoliated $MoS_2$. *Nano Lett.* **2011**, *11*, 5111–5116. [CrossRef]
21. Novoselov, K.S.; Geim, A.K.; Morozov, S.V.; Jiang, D.; Zhang, Y.; Dubonos, S.V.; Grigorieva, I.V.; Firsov, A.A. Electric Field Effect in Atomically Thin Carbon Films. *Science* **2004**, *306*, 666–669. [CrossRef]
22. Magda, G.Z.; Pető, J.; Dobrik, G.; Hwang, C.; Biró, L.P.; Tapasztó, L. Exfoliation of Large-Area Transition Metal Chalcogenide Single Layers. *Sci. Rep.* **2015**, *5*, 14714. [CrossRef] [PubMed]
23. Dines, M.B. Lithium Intercalation via N-Butyl Lithium of the Layered Transition Metal Dichalcogenides. *Mater. Res. Bull.* **1975**, *10*, 5. [CrossRef]
24. Li, L.; Yu, Y.; Ye, G.J.; Ge, Q.; Ou, X.; Wu, H.; Feng, D.; Chen, X.H.; Zhang, Y. Black Phosphorus Field-Effect Transistors. *Nat. Nanotechnol.* **2014**, *9*, 372–377. [CrossRef] [PubMed]
25. Eda, G.; Maier, S.A. Two-Dimensional Crystals: Managing Light for Optoelectronics. *ACS Nano* **2013**, *7*, 5660–5665. [CrossRef]
26. Kojima, A.; Teshima, K.; Shirai, Y.; Miyasaka, T. Organometal Halide Perovskites as Visible-Light Sensitizers for Photovoltaic Cells. *J. Am. Chem. Soc.* **2009**, *131*, 6050–6051. [CrossRef]
27. Jeong, J.; Kim, M.; Seo, J.; Lu, H.; Ahlawat, P.; Mishra, A.; Yang, Y.; Hope, M.A.; Eickemeyer, F.T.; Kim, M.; et al. Pseudo-Halide Anion Engineering for $\alpha$-$FAPbI_3$ Perovskite Solar Cells. *Nature* **2021**, *592*, 381–385. [CrossRef]
28. Yang, Z.; Wang, M.; Li, J.; Dou, J.; Qiu, H.; Shao, J. Spray-Coated $CsPbBr_3$ Quantum Dot Films for Perovskite Photodiodes. *ACS Appl. Mater. Interfaces* **2018**, *10*, 26387–26395. [CrossRef]
29. Liang, F.-X.; Wang, J.-Z.; Zhang, Z.-X.; Wang, Y.-Y.; Gao, Y.; Luo, L.-B. Broadband, Ultrafast, Self-Driven Photodetector Based on Cs-Doped $FAPbI_3$ Perovskite Thin Film. *Adv. Opt. Mater.* **2017**, *5*, 1700654. [CrossRef]
30. D'Innocenzo, V.; Grancini, G.; Alcocer, M.J.P.; Kandada, A.R.S.; Stranks, S.D.; Lee, M.M.; Lanzani, G.; Snaith, H.J.; Petrozza, A. Excitons versus Free Charges in Organo-Lead Tri-Halide Perovskites. *Nat. Commun.* **2014**, *5*, 3586. [CrossRef]
31. Stranks, S.D.; Eperon, G.E.; Grancini, G.; Menelaou, C.; Alcocer, M.J.P.; Leijtens, T.; Herz, L.M.; Petrozza, A.; Snaith, H.J. Electron-Hole Diffusion Lengths Exceeding 1 Micrometer in an Organometal Trihalide Perovskite Absorber. *Science* **2013**, *342*, 341–344. [CrossRef]
32. Yang, X.; Luo, D.; Xiang, Y.; Zhao, L.; Anaya, M.; Shen, Y.; Wu, J.; Yang, W.; Chiang, Y.-H.; Tu, Y.; et al. Buried Interfaces in Halide Perovskite Photovoltaics. *Adv. Mater* **2021**, *10*, 2006435. [CrossRef] [PubMed]
33. Zhang, Z.; Wang, S.; Liu, X.; Chen, Y.; Su, C.; Tang, Z.; Li, Y.; Xing, G. Metal Halide Perovskite/2D Material Heterostructures: Syntheses and Applications. *Small Methods* **2021**, *5*, 2000937. [CrossRef] [PubMed]
34. Bolotin, K.I.; Sikes, K.J.; Jiang, Z.; Klima, M.; Fudenberg, G.; Hone, J.; Kim, P.; Stormer, H.L. Ultrahigh Electron Mobility in Suspended Graphene. *Solid State Commun.* **2008**, *146*, 351–355. [CrossRef]
35. Novoselov, K.S.; Geim, A.K.; Morozov, S.V.; Jiang, D.; Katsnelson, M.I.; Grigorieva, I.V.; Dubonos, S.V.; Firsov, A.A. Two-Dimensional Gas of Massless Dirac Fermions in Graphene. *Nature* **2005**, *438*, 197–200. [CrossRef] [PubMed]
36. Zhang, Y.; Tan, Y.-W.; Stormer, H.L.; Kim, P. Experimental Observation of the Quantum Hall Effect and Berry's Phase in Graphene. *Nature* **2005**, *438*, 201–204. [CrossRef] [PubMed]
37. Semenoff, G.W. Condensed-Matter Simulation of a Three-Dimensional Anomaly. *Phys. Rev. Lett.* **1984**, *53*, 2449–2452. [CrossRef]
38. Novoselov, K.S. Nobel Lecture: Graphene: Materials in the Flatland. *Rev. Mod. Phys.* **2011**, *83*, 837–849. [CrossRef]
39. Chua, C.K.; Pumera, M. Chemical Reduction of Graphene Oxide: A Synthetic Chemistry Viewpoint. *Chem. Soc. Rev.* **2014**, *43*, 291–312. [CrossRef]
40. Chandrashekar, B.N.; Deng, B.; Smitha, A.S.; Chen, Y.; Tan, C.; Zhang, H.; Peng, H.; Liu, Z. Roll-to-Roll Green Transfer of CVD Graphene onto Plastic for a Transparent and Flexible Triboelectric Nanogenerator. *Adv. Mater.* **2015**, *27*, 5210–5216. [CrossRef]
41. Moon, I.K.; Lee, J.; Ruoff, R.S.; Lee, H. Reduced Graphene Oxide by Chemical Graphitization. *Nat. Commun.* **2010**, *1*, 73. [CrossRef]
42. Ambrosi, A.; Chua, C.K.; Bonanni, A.; Pumera, M. Lithium Aluminum Hydride as Reducing Agent for Chemically Reduced Graphene Oxides. *Chem. Mater.* **2012**, *24*, 2292–2298. [CrossRef]
43. Feng, H.; Cheng, R.; Zhao, X.; Duan, X.; Li, J. A Low-Temperature Method to Produce Highly Reduced Graphene Oxide. *Nat. Commun.* **2013**, *4*, 1539. [CrossRef] [PubMed]
44. Li, X.; Cai, W.; An, J.; Kim, S.; Nah, J.; Yang, D.; Piner, R.; Velamakanni, A.; Jung, I.; Tutuc, E.; et al. Large-Area Synthesis of High-Quality and Uniform Graphene Films on Copper Foils. *Science* **2009**, *324*, 1312–1314. [CrossRef] [PubMed]
45. Kim, K.S.; Zhao, Y.; Jang, H.; Lee, S.Y.; Kim, J.M.; Kim, K.S.; Ahn, J.-H.; Kim, P.; Choi, J.-Y.; Hong, B.H. Large-Scale Pattern Growth of Graphene Films for Stretchable Transparent Electrodes. *Nature* **2009**, *457*, 706–710. [CrossRef]

46. Bae, S.; Kim, H.; Lee, Y.; Xu, X.; Park, J.-S.; Zheng, Y.; Balakrishnan, J.; Lei, T.; Ri Kim, H.; Song, Y.I.; et al. Roll-to-Roll Production of 30-Inch Graphene Films for Transparent Electrodes. *Nat. Nanotechnol.* **2010**, *5*, 574–578. [CrossRef]
47. Bosi, M. Growth and Synthesis of Mono and Few-Layers Transition Metal Dichalcogenides by Vapour Techniques: A Review. *RSC Adv.* **2015**, *5*, 75500–75518. [CrossRef]
48. Yue, R.; Barton, A.T.; Zhu, H.; Azcatl, A.; Pena, L.F.; Wang, J.; Peng, X.; Lu, N.; Cheng, L.; Addou, R.; et al. $HfSe_2$ Thin Films: 2D Transition Metal Dichalcogenides Grown by Molecular Beam Epitaxy. *ACS Nano* **2015**, *9*, 474–480. [CrossRef]
49. Zeng, Z.; Yin, Z.; Huang, X.; Li, H.; He, Q.; Lu, G.; Boey, F.; Zhang, H. Single-Layer Semiconducting Nanosheets: High-Yield Preparation and Device Fabrication. *Angew. Chem.* **2011**, *123*, 11289–11293. [CrossRef]
50. Li, H.; Wu, J.; Yin, Z.; Zhang, H. Preparation and Applications of Mechanically Exfoliated Single-Layer and Multilayer $MoS_2$ and $WSe_2$ Nanosheets. *Acc. Chem. Res.* **2014**, *47*, 1067–1075. [CrossRef]
51. Jeong, S.; Yoo, D.; Ahn, M.; Miró, P.; Heine, T.; Cheon, J. Tandem Intercalation Strategy for Single-Layer Nanosheets as an Effective Alternative to Conventional Exfoliation Processes. *Nat. Commun.* **2015**, *6*, 5763. [CrossRef]
52. Raza, A.; Hassan, J.Z.; Ikram, M.; Ali, S.; Farooq, U.; Khan, Q.; Maqbool, M. Advances in Liquid-Phase and Intercalation Exfoliations of Transition Metal Dichalcogenides to Produce 2D Framework. *Adv. Mater. Interfaces* **2021**, *8*, 2002205. [CrossRef]
53. Coleman, J.N.; Lotya, M.; O'Neill, A.; Bergin, S.D.; King, P.J.; Khan, U.; Young, K.; Gaucher, A.; De, S.; Smith, R.J.; et al. Two-Dimensional Nanosheets Produced by Liquid Exfoliation of Layered Materials. *Science* **2011**, *331*, 568–571. [CrossRef] [PubMed]
54. Chang, Y.-H.; Zhang, W.; Zhu, Y.; Han, Y.; Pu, J.; Chang, J.-K.; Hsu, W.-T.; Huang, J.-K.; Hsu, C.-L.; Chiu, M.-H.; et al. Monolayer $MoSe_2$ Grown by Chemical Vapor Deposition for Fast Photodetection. *ACS Nano* **2014**, *8*, 8582–8590. [CrossRef] [PubMed]
55. Zhang, Y.; Zhang, Y.; Ji, Q.; Ju, J.; Yuan, H.; Shi, J.; Gao, T.; Ma, D.; Liu, M.; Chen, Y.; et al. Controlled Growth of High-Quality Monolayer $WS_2$ Layers on Sapphire and Imaging Its Grain Boundary. *ACS Nano* **2013**, *7*, 8963–8971. [CrossRef]
56. Liu, B.; Fathi, M.; Chen, L.; Abbas, A.; Ma, Y.; Zhou, C. Chemical Vapor Deposition Growth of Monolayer $WSe_2$ with Tunable Device Characteristics and Growth Mechanism Study. *ACS Nano* **2015**, *9*, 6119–6127. [CrossRef]
57. Orofeo, C.M.; Suzuki, S.; Sekine, Y.; Hibino, H. Scalable Synthesis of Layer-Controlled $WS_2$ and $MoS_2$ Sheets by Sulfurization of Thin Metal Films. *Appl. Phys. Lett.* **2014**, *105*, 083112. [CrossRef]
58. Jin, Z.; Shin, S.; Kwon, D.H.; Han, S.-J.; Min, Y.-S. Novel Chemical Route for Atomic Layer Deposition of $MoS_2$ Thin Film on $SiO_2$/Si Substrate. *Nanoscale* **2014**, *6*, 14453–14458. [CrossRef]
59. Tan, Z.-K.; Moghaddam, R.S.; Lai, M.L.; Docampo, P.; Higler, R.; Deschler, F.; Price, M.; Sadhanala, A.; Pazos, L.M.; Credgington, D.; et al. Bright Light-Emitting Diodes Based on Organometal Halide Perovskite. *Nat. Nanotechnol.* **2014**, *9*, 687–692. [CrossRef]
60. Fang, Y.; Dong, Q.; Shao, Y.; Yuan, Y.; Huang, J. Highly Narrowband Perovskite Single-Crystal Photodetectors Enabled by Surface-Charge Recombination. *Nat. Photonics* **2015**, *9*, 679–686. [CrossRef]
61. Zhao, W.; Lin, H.; Li, Y.; Wang, D.; Wang, J.; Liu, Z.; Yuan, N.; Ding, J.; Wang, Q.; Liu, S. Symmetrical Acceptor–Donor–Acceptor Molecule as a Versatile Defect Passivation Agent toward Efficient $FA_{0.85}MA_{0.15}PbI_3$ Perovskite Solar Cells. *Adv. Funct. Mater.* **2022**, *32*, 2112032. [CrossRef]
62. Han, Y.; Xie, H.; Lim, E.L.; Bi, D. Review of Two-Step Method for Lead Halide Perovskite Solar Cells. *Sol. RRL* **2022**, *6*, 2101007. [CrossRef]
63. Vaynzof, Y. The Future of Perovskite Photovoltaics—Thermal Evaporation or Solution Processing? *Adv. Energy Mater.* **2020**, *10*, 2003073. [CrossRef]
64. Chiang, C.-H.; Lin, J.-W.; Wu, C.-G. One-Step Fabrication of a Mixed-Halide Perovskite Film for a High-Efficiency Inverted Solar Cell and Module. *J. Mater. Chem. A* **2016**, *4*, 13525–13533. [CrossRef]
65. Chen, Q.; Deng, K.; Shen, Y.; Li, L. Stable One Dimensional (1D)/Three Dimensional (3D) Perovskite Solar Cell with an Efficiency Exceeding 23%. *InfoMat* **2022**, *4*, e12303. [CrossRef]
66. Wang, J.; Lin, D.; Chen, Y.; Luo, S.; Ke, L.; Ren, X.; Cui, S.; Zhang, L.; Li, Z.; Meng, K.; et al. Suppressing the Excessive Solvated Phase for Dion–Jacobson Perovskites with Improved Crystallinity and Vertical Orientation. *Sol. RRL* **2020**, *4*, 2000371. [CrossRef]
67. Zhang, F.; Zhong, H.; Chen, C.; Wu, X.; Hu, X.; Huang, H.; Han, J.; Zou, B.; Dong, Y. Brightly Luminescent and Color-Tunable Colloidal $CH_3NH_3PbX_3$ (X = Br, I, Cl) Quantum Dots: Potential Alternatives for Display Technology. *ACS Nano* **2015**, *9*, 4533–4542. [CrossRef]
68. Protesescu, L.; Yakunin, S.; Bodnarchuk, M.I.; Krieg, F.; Caputo, R.; Hendon, C.H.; Yang, R.X.; Walsh, A.; Kovalenko, M.V. Nanocrystals of Cesium Lead Halide Perovskites ($CsPbX_3$, X = Cl, Br, and I): Novel Optoelectronic Materials Showing Bright Emission with Wide Color Gamut. *Nano Lett.* **2015**, *15*, 3692–3696. [CrossRef]
69. De Roo, J.; Ibáñez, M.; Geiregat, P.; Nedelcu, G.; Walravens, W.; Maes, J.; Martins, J.C.; Van Driessche, I.; Kovalenko, M.V.; Hens, Z. Highly Dynamic Ligand Binding and Light Absorption Coefficient of Cesium Lead Bromide Perovskite Nanocrystals. *ACS Nano* **2016**, *10*, 2071–2081. [CrossRef]
70. Soe, C.M.M.; Stoumpos, C.C.; Kepenekian, M.; Traoré, B.; Tsai, H.; Nie, W.; Wang, B.; Katan, C.; Seshadri, R.; Mohite, A.D.; et al. New Type of 2D Perovskites with Alternating Cations in the Interlayer Space, $(C(NH_2)_3)(CH_3\ NH_3)_nPb_nI_{3n+1}$: Structure, Properties, and Photovoltaic Performance. *J. Am. Chem. Soc.* **2017**, *139*, 16297–16309. [CrossRef]
71. Gong, X.; Guan, L.; Pan, H.; Sun, Q.; Zhao, X.; Li, H.; Pan, H.; Shen, Y.; Shao, Y.; Sun, L.; et al. Highly Efficient Perovskite Solar Cells via Nickel Passivation. *Adv. Funct. Mater.* **2018**, *28*, 1804286. [CrossRef]

72. Zhi, L.; Li, Y.; Cao, X.; Li, Y.; Cui, X.; Ci, L.; Wei, J. Dissolution and Recrystallization of Perovskite Induced by N-Methyl-2-Pyrrolidone in a Closed Steam Annealing Method. *J. Energy Chem.* **2019**, *30*, 78–83. [CrossRef]
73. Noel, N.K.; Abate, A.; Stranks, S.D.; Parrott, E.S.; Burlakov, V.M.; Goriely, A.; Snaith, H.J. Enhanced Photoluminescence and Solar Cell Performance via Lewis Base Passivation of Organic–Inorganic Lead Halide Perovskites. *ACS Nano* **2014**, *8*, 9815–9821. [CrossRef] [PubMed]
74. Pham, H.T.; Yin, Y.; Andersson, G.; Weber, K.J.; Duong, T.; Wong-Leung, J. Unraveling the Influence of CsCl/MACl on the Formation of Nanotwins, Stacking Faults and Cubic Supercell Structure in FA-Based Perovskite Solar Cells. *Nano Energy* **2021**, *87*, 106226. [CrossRef]
75. Yang, L.; Gao, Y.; Wu, Y.; Xue, X.; Wang, F.; Sui, Y.; Sun, Y.; Wei, M.; Liu, X.; Liu, H. Novel Insight into the Role of Chlorobenzene Antisolvent Engineering for Highly Efficient Perovskite Solar Cells: Gradient Diluted Chlorine Doping. *ACS Appl. Mater. Interfaces* **2019**, *11*, 792–801. [CrossRef] [PubMed]
76. Xiao, M.; Zhao, L.; Geng, M.; Li, Y.; Dong, B.; Xu, Z.; Wan, L.; Li, W.; Wang, S. Selection of an Anti-Solvent for Efficient and Stable Cesium-Containing Triple Cation Planar Perovskite Solar Cells. *Nanoscale* **2018**, *10*, 12141–12148. [CrossRef]
77. Jeon, N.J.; Noh, J.H.; Kim, Y.C.; Yang, W.S.; Ryu, S.; Seok, S.I. Solvent Engineering for High-Performance Inorganic–Organic Hybrid Perovskite Solar Cells. *Nat. Mater.* **2014**, *13*, 897–903. [CrossRef] [PubMed]
78. Zhang, W. Ethyl Acetate Green Antisolvent Process for High-Performance Planar Low-Temperature $SnO_2$-Based Perovskite Solar Cells Made in Ambient Air. *Chem. Eng. J.* **2020**, *79*, 122298. [CrossRef]
79. Taylor, A.D.; Sun, Q.; Goetz, K.P.; An, Q.; Schramm, T.; Hofstetter, Y.; Litterst, M.; Paulus, F.; Vaynzof, Y. A General Approach to High-Efficiency Perovskite Solar Cells by Any Antisolvent. *Nat. Commun.* **2021**, *12*, 1878. [CrossRef]
80. Lohmann, K.B.; Patel, J.B.; Rothmann, M.U.; Xia, C.Q.; Oliver, R.D.J.; Herz, L.M.; Snaith, H.J.; Johnston, M.B. Control over Crystal Size in Vapor Deposited Metal-Halide Perovskite Films. *ACS Energy Lett.* **2020**, *5*, 710–717. [CrossRef]
81. Juarez-Perez, E.J.; Hawash, Z.; Raga, S.R.; Ono, L.K.; Qi, Y. Thermal Degradation of $CH_3$ $NH_3$ $PbI_3$ Perovskite into $NH_3$ and $CH_3I$ Gases Observed by Coupled Thermogravimetry–Mass Spectrometry Analysis. *Energy Environ. Sci.* **2016**, *9*, 3406–3410. [CrossRef]
82. Lohmann, K.B.; Motti, S.G.; Oliver, R.D.J.; Ramadan, A.J.; Sansom, H.C.; Yuan, Q.; Elmestekawy, K.A.; Patel, J.B.; Ball, J.M.; Herz, L.M.; et al. Solvent-Free Method for Defect Reduction and Improved Performance of p-i-n Vapor-Deposited Perovskite Solar Cells. *ACS Energy Lett.* **2022**, *7*, 1903–1911. [CrossRef]
83. Arciniegas, M.P.; Castelli, A.; Piazza, S.; Dogan, S.; Ceseracciu, L.; Krahne, R.; Duocastella, M.; Manna, L. Laser-Induced Localized Growth of Methylammonium Lead Halide Perovskite Nano- and Microcrystals on Substrates. *Adv. Funct. Mater.* **2017**, *27*, 1701613. [CrossRef]
84. Zou, C.; Zheng, J.; Chang, C.; Majumdar, A.; Lin, L.Y. Nonvolatile Rewritable Photomemory Arrays Based on Reversible Phase-Change Perovskite for Optical Information Storage. *Adv. Opt. Mater.* **2019**, *7*, 1900558. [CrossRef]
85. Mao, L.; Ke, W.; Pedesseau, L.; Wu, Y.; Katan, C.; Even, J.; Wasielewski, M.R.; Stoumpos, C.C.; Kanatzidis, M.G. Hybrid Dion–Jacobson 2D Lead Iodide Perovskites. *J. Am. Chem. Soc.* **2018**, *140*, 3775–3783. [CrossRef] [PubMed]
86. Billing, D.G.; Lemmerer, A. Synthesis, Characterization and Phase Transitions in the Inorganic–Organic Layered Perovskite-Type Hybrids $[(C_nH_{2n+1}NH_3)_2PbI_4]$, $n$ = 4, 5 and 6. *Acta Crystallogr. B* **2007**, *63*, 735–747. [CrossRef] [PubMed]
87. Li, X.; Hoffman, J.; Ke, W.; Chen, M.; Tsai, H.; Nie, W.; Mohite, A.D.; Kepenekian, M.; Katan, C.; Even, J.; et al. Two-Dimensional Halide Perovskites Incorporating Straight Chain Symmetric Diammonium Ions, $(NH_3C_mH_{2m}NH_3)(CH_3NH_3)_{n-1}Pb_nI_{3n+1}$ ($m$ = 4–9; $n$ = 1–4). *J. Am. Chem. Soc.* **2018**, *140*, 12226–12238. [CrossRef]
88. Lemmerer, A.; Billing, D.G. Lead Halide Inorganic–Organic Hybrids Incorporating Diammonium Cations. *CrystEngComm* **2012**, *14*, 1954. [CrossRef]
89. Mao, L.; Stoumpos, C.C.; Kanatzidis, M.G. Two-Dimensional Hybrid Halide Perovskites: Principles and Promises. *J. Am. Chem. Soc.* **2019**, *141*, 1171–1190. [CrossRef]
90. Lu, D.; Lv, G.; Xu, Z.; Dong, Y.; Ji, X.; Liu, Y. Thiophene-Based Two-Dimensional Dion–Jacobson Perovskite Solar Cells with over 15% Efficiency. *J. Am. Chem. Soc.* **2020**, *142*, 11114–11122. [CrossRef]
91. Stoumpos, C.C.; Soe, C.M.M.; Tsai, H.; Nie, W.; Blancon, J.-C.; Cao, D.H.; Liu, F.; Traoré, B.; Katan, C.; Even, J.; et al. High Members of the 2D Ruddlesden-Popper Halide Perovskites: Synthesis, Optical Properties, and Solar Cells of $(CH_3(CH_2)_3NH_3)_2(CH_3NH_3)_4Pb_5I_{16}$. *Chem* **2017**, *2*, 427–440. [CrossRef]
92. Zhang, X.; Wu, G.; Fu, W.; Qin, M.; Yang, W.; Yan, J.; Zhang, Z.; Lu, X.; Chen, H. Orientation Regulation of Phenylethylammonium Cation Based 2D Perovskite Solar Cell with Efficiency Higher Than 11%. *Adv. Energy Mater.* **2018**, *8*, 1702498. [CrossRef]
93. Marimuthu, T.; Yuvakkumar, R.; Kumar, P.S.; Vo, D.-V.N.; Xu, X.; Xu, G. Two-Dimensional Hybrid Perovskite Solar Cells: A Review. *Environ. Chem. Lett.* **2022**, *20*, 189–210. [CrossRef]
94. Liang, D.; Dong, C.; Cai, L.; Su, Z.; Zang, J.; Wang, C.; Wang, X.; Zou, Y.; Li, Y.; Chen, L.; et al. Unveiling Crystal Orientation in Quasi-2D Perovskite Films by In Situ GIWAXS for High-Performance Photovoltaics. *Small* **2021**, *17*, 2100972. [CrossRef] [PubMed]
95. Quan, L.N.; Zhao, Y.; García de Arquer, F.P.; Sabatini, R.; Walters, G.; Voznyy, O.; Comin, R.; Li, Y.; Fan, J.Z.; Tan, H.; et al. Tailoring the Energy Landscape in Quasi-2D Halide Perovskites Enables Efficient Green-Light Emission. *Nano Lett.* **2017**, *17*, 3701–3709. [CrossRef]
96. Ma, D.; Lin, K.; Dong, Y.; Choubisa, H.; Proppe, A.H.; Wu, D.; Wang, Y.-K.; Chen, B.; Li, P.; Fan, J.Z.; et al. Distribution Control Enables Efficient Reduced-Dimensional Perovskite LEDs. *Nature* **2021**, *599*, 594–598. [CrossRef]

97. Proppe, A.H.; Wei, M.; Chen, B.; Quintero-Bermudez, R.; Kelley, S.O.; Sargent, E.H. Photochemically Cross-Linked Quantum Well Ligands for 2D/3D Perovskite Photovoltaics with Improved Photovoltage and Stability. *J. Am. Chem. Soc.* **2019**, *141*, 14180–14189. [CrossRef]
98. Teale, S.; Proppe, A.H.; Jung, E.H.; Johnston, A.; Parmar, D.H.; Chen, B.; Hou, Y.; Kelley, S.O.; Sargent, E.H. Dimensional Mixing Increases the Efficiency of 2D/3D Perovskite Solar Cells. *J. Phys. Chem. Lett.* **2020**, *11*, 5115–5119. [CrossRef]
99. Chen, H.; Teale, S.; Chen, B.; Hou, Y.; Grater, L.; Zhu, T.; Bertens, K.; Park, S.M.; Atapattu, H.R.; Gao, Y.; et al. Quantum-Size-Tuned Heterostructures Enable Efficient and Stable Inverted Perovskite Solar Cells. *Nat. Photonics* **2022**, *16*, 352–358. [CrossRef]
100. Liu, C.; Sun, J.; Tan, W.L.; Lu, J.; Gengenbach, T.R.; McNeill, C.R.; Ge, Z.; Cheng, Y.-B.; Bach, U. Alkali Cation Doping for Improving the Structural Stability of 2D Perovskite in 3D/2D PSCs. *Nano Lett.* **2020**, *20*, 1240–1251. [CrossRef]
101. Yoo, J.J.; Wieghold, S.; Sponseller, M.C.; Chua, M.R.; Bertram, S.N.; Hartono, N.T.P.; Tresback, J.S.; Hansen, E.C.; Correa-Baena, J.-P.; Bulović, V.; et al. An Interface Stabilized Perovskite Solar Cell with High Stabilized Efficiency and Low Voltage Loss. *Energy Environ. Sci.* **2019**, *12*, 2192–2199. [CrossRef]
102. Jang, Y.-W.; Lee, S.; Yeom, K.M.; Jeong, K.; Choi, K.; Choi, M.; Noh, J.H. Intact 2D/3D Halide Junction Perovskite Solar Cells via Solid-Phase in-Plane Growth. *Nat. Energy* **2021**, *6*, 63–71. [CrossRef]
103. Huang, X.; Guo, Q.; Yang, D.; Xiao, X.; Liu, X.; Xia, Z.; Fan, F.; Qiu, J.; Dong, G. Reversible 3D Laser Printing of Perovskite Quantum Dots inside a Transparent Medium. *Nat. Photonics* **2020**, *14*, 82–88. [CrossRef]
104. Schmidt, L.C.; Pertegás, A.; González-Carrero, S.; Malinkiewicz, O.; Agouram, S.; Mínguez Espallargas, G.; Bolink, H.J.; Galian, R.E.; Pérez-Prieto, J. Nontemplate Synthesis of $CH_3NH_3PbBr_3$ Perovskite Nanoparticles. *J. Am. Chem. Soc.* **2014**, *136*, 850–853. [CrossRef] [PubMed]
105. Gonzalez-Carrero, S.; Galian, R.E.; Pérez-Prieto, J. Maximizing the Emissive Properties of $CH_3NH_3PbBr_3$ Perovskite Nanoparticles. *J. Mater. Chem. A* **2015**, *3*, 9187–9193. [CrossRef]
106. Yettapu, G.R.; Talukdar, D.; Sarkar, S.; Swarnkar, A.; Nag, A.; Ghosh, P.; Mandal, P. Terahertz Conductivity within Colloidal $CsPbBr_3$ Perovskite Nanocrystals: Remarkably High Carrier Mobilities and Large Diffusion Lengths. *Nano Lett.* **2016**, *16*, 4838–4848. [CrossRef]
107. Zou, T.; Liu, X.; Qiu, R.; Wang, Y.; Huang, S.; Liu, C.; Dai, Q.; Zhou, H. Enhanced UV-C Detection of Perovskite Photodetector Arrays via Inorganic $CsPbBr_3$ Quantum Dot Down-Conversion Layer. *Adv. Opt. Mater.* **2019**, *7*, 1801812. [CrossRef]
108. Lu, J.; Sheng, X.; Tong, G.; Yu, Z.; Sun, X.; Yu, L.; Xu, X.; Wang, J.; Xu, J.; Shi, Y.; et al. Ultrafast Solar-Blind Ultraviolet Detection by Inorganic Perovskite $CsPbX_3$ Quantum Dots Radial Junction Architecture. *Adv. Mater.* **2017**, *29*, 1700400. [CrossRef]
109. Li, J.; Xu, L.; Wang, T.; Song, J.; Chen, J.; Xue, J.; Dong, Y.; Cai, B.; Shan, Q.; Han, B.; et al. 50-Fold EQE Improvement up to 6.27% of Solution-Processed All-Inorganic Perovskite $CsPbBr_3$ QLEDs via Surface Ligand Density Control. *Adv. Mater.* **2017**, *29*, 1603885. [CrossRef]
110. Yan, F.; Xing, J.; Xing, G.; Quan, L.; Tan, S.T.; Zhao, J.; Su, R.; Zhang, L.; Chen, S.; Zhao, Y.; et al. Highly Efficient Visible Colloidal Lead-Halide Perovskite Nanocrystal Light-Emitting Diodes. *Nano Lett.* **2018**, *18*, 3157–3164. [CrossRef]
111. Song, J.; Fang, T.; Li, J.; Xu, L.; Zhang, F.; Han, B.; Shan, Q.; Zeng, H. Organic–Inorganic Hybrid Passivation Enables Perovskite QLEDs with an EQE of 16.48%. *Adv. Mater.* **2018**, *30*, 1805409. [CrossRef]
112. Swarnkar, A.; Marshall, A.R.; Sanehira, E.M.; Chernomordik, B.D.; Moore, D.T.; Christians, J.A.; Chakrabarti, T.; Luther, J.M. Quantum Dot–Induced Phase Stabilization of α-$CsPbI_3$ Perovskite for High-Efficiency Photovoltaics. *Science* **2016**, *354*, 92–95. [CrossRef] [PubMed]
113. Nedelcu, G.; Protesescu, L.; Yakunin, S.; Bodnarchuk, M.I.; Grotevent, M.J.; Kovalenko, M.V. Fast Anion-Exchange in Highly Luminescent Nanocrystals of Cesium Lead Halide Perovskites ($CsPbX_3$, X = Cl, Br, I). *Nano Lett.* **2015**, *15*, 5635–5640. [CrossRef] [PubMed]
114. Jia, D.; Chen, J.; Mei, X.; Fan, W.; Luo, S.; Yu, M.; Liu, J.; Zhang, X. Surface Matrix Curing of Inorganic $CsPbI_3$ Perovskite Quantum Dots for Solar Cells with Efficiency over 16%. *Energy Environ. Sci.* **2021**, *14*, 4599–4609. [CrossRef]
115. Lignos, I.; Stavrakis, S.; Nedelcu, G.; Protesescu, L.; deMello, A.J.; Kovalenko, M.V. Synthesis of Cesium Lead Halide Perovskite Nanocrystals in a Droplet-Based Microfluidic Platform: Fast Parametric Space Mapping. *Nano Lett.* **2016**, *16*, 1869–1877. [CrossRef]
116. Krieg, F.; Ochsenbein, S.T.; Yakunin, S.; ten Brinck, S.; Aellen, P.; Süess, A.; Clerc, B.; Guggisberg, D.; Nazarenko, O.; Shynkarenko, Y.; et al. Colloidal $CsPbX_3$ (X = Cl, Br, I) Nanocrystals 2.0: Zwitterionic Capping Ligands for Improved Durability and Stability. *ACS Energy Lett.* **2018**, *3*, 641–646. [CrossRef]
117. Shynkarenko, Y.; Bodnarchuk, M.I.; Bernasconi, C.; Berezovska, Y.; Verteletskyi, V.; Ochsenbein, S.T.; Kovalenko, M.V. Direct Synthesis of Quaternary Alkylammonium-Capped Perovskite Nanocrystals for Efficient Blue and Green Light-Emitting Diodes. *ACS Energy Lett.* **2019**, *4*, 2703–2711. [CrossRef]
118. Li, G.; Huang, J.; Zhu, H.; Li, Y.; Tang, J.-X.; Jiang, Y. Surface Ligand Engineering for Near-Unity Quantum Yield Inorganic Halide Perovskite QDs and High-Performance QLEDs. *Chem. Mater.* **2018**, *30*, 6099–6107. [CrossRef]
119. Dai, J.; Xi, J.; Li, L.; Zhao, J.; Shi, Y.; Zhang, W.; Ran, C.; Jiao, B.; Hou, X.; Duan, X.; et al. Charge Transport between Coupling Colloidal Perovskite Quantum Dots Assisted by Functional Conjugated Ligands. *Angew. Chem. Int. Ed.* **2018**, *57*, 5754–5758. [CrossRef]
120. Liu, F.; Zhang, Y.; Ding, C.; Kobayashi, S.; Izuishi, T.; Nakazawa, N.; Toyoda, T.; Ohta, T.; Hayase, S.; Minemoto, T.; et al. Highly Luminescent Phase-Stable $CsPbI_3$ Perovskite Quantum Dots Achieving Near 100% Absolute Photoluminescence Quantum Yield. *ACS Nano* **2017**, *11*, 10373–10383. [CrossRef]

121. Hao, M.; Bai, Y.; Zeiske, S.; Ren, L.; Liu, J.; Yuan, Y.; Zarrabi, N.; Cheng, N.; Ghasemi, M.; Chen, P.; et al. Ligand-Assisted Cation-Exchange Engineering for High-Efficiency Colloidal $Cs_{1-x}FA_xPbI_3$ Quantum Dot Solar Cells with Reduced Phase Segregation. *Nat. Energy* **2020**, *5*, 79–88. [CrossRef]
122. Wheeler, L.M.; Sanehira, E.M.; Marshall, A.R.; Schulz, P.; Suri, M.; Anderson, N.C.; Christians, J.A.; Nordlund, D.; Sokaras, D.; Kroll, T.; et al. Targeted Ligand-Exchange Chemistry on Cesium Lead Halide Perovskite Quantum Dots for High-Efficiency Photovoltaics. *J. Am. Chem. Soc.* **2018**, *140*, 10504–10513. [CrossRef] [PubMed]
123. Chen, J.; Jia, D.; Qiu, J.; Zhuang, R.; Hua, Y.; Zhang, X. Multidentate Passivation Crosslinking Perovskite Quantum Dots for Efficient Solar Cells. *Nano Energy* **2022**, *96*, 107140. [CrossRef]
124. Ling, X.; Zhou, S.; Yuan, J.; Shi, J.; Qian, Y.; Larson, B.W.; Zhao, Q.; Qin, C.; Li, F.; Shi, G.; et al. 14.1% $CsPbI_3$ Perovskite Quantum Dot Solar Cells via Cesium Cation Passivation. *Adv. Energy Mater.* **2019**, *9*, 1900721. [CrossRef]
125. Ling, X.; Yuan, J.; Zhang, X.; Qian, Y.; Zakeeruddin, S.M.; Larson, B.W.; Zhao, Q.; Shi, J.; Yang, J.; Ji, K.; et al. Guanidinium-Assisted Surface Matrix Engineering for Highly Efficient Perovskite Quantum Dot Photovoltaics. *Adv. Mater.* **2020**, *32*, 2001906. [CrossRef] [PubMed]
126. Kim, J.; Cho, S.; Dinic, F.; Choi, J.; Choi, C.; Jeong, S.M.; Lee, J.-S.; Voznyy, O.; Ko, M.J.; Kim, Y. Hydrophobic Stabilizer-Anchored Fully Inorganic Perovskite Quantum Dots Enhance Moisture Resistance and Photovoltaic Performance. *Nano Energy* **2020**, *75*, 104985. [CrossRef]
127. Wi, S.; Kim, H.; Chen, M.; Nam, H.; Guo, L.J.; Meyhofer, E.; Liang, X. Enhancement of Photovoltaic Response in Multilayer $MoS_2$ Induced by Plasma Doping. *ACS Nano* **2014**, *8*, 5270–5281. [CrossRef] [PubMed]
128. Guo, Q.; Pospischil, A.; Bhuiyan, M.; Jiang, H.; Tian, H.; Farmer, D.; Deng, B.; Li, C.; Han, S.-J.; Wang, H.; et al. Black Phosphorus Mid-Infrared Photodetectors with High Gain. *Nano Lett.* **2016**, *16*, 4648–4655. [CrossRef]
129. McVay, E.; Zubair, A.; Lin, Y.; Nourbakhsh, A.; Palacios, T. Impact of $Al_2O_3$ Passivation on the Photovoltaic Performance of Vertical $WSe_2$ Schottky Junction Solar Cells. *ACS Appl. Mater. Interfaces* **2020**, *12*, 57987–57995. [CrossRef]
130. Nassiri Nazif, K.; Daus, A.; Hong, J.; Lee, N.; Vaziri, S.; Kumar, A.; Nitta, F.; Chen, M.E.; Kananian, S.; Islam, R.; et al. High-Specific-Power Flexible Transition Metal Dichalcogenide Solar Cells. *Nat. Commun.* **2021**, *12*, 7034. [CrossRef]
131. Wang, X.; Wang, P.; Wang, J.; Hu, W.; Zhou, X.; Guo, N.; Huang, H.; Sun, S.; Shen, H.; Lin, T.; et al. Ultrasensitive and Broadband $MoS_2$ Photodetector Driven by Ferroelectrics. *Adv. Mater.* **2015**, *27*, 6575–6581. [CrossRef]
132. Kim, S.J.; Kim, D.; Min, B.K.; Yi, Y.; Mondal, S.; Nguyen, V.; Hwang, J.; Suh, D.; Cho, K.; Choi, C. Bandgap Tuned $WS_2$ Thin-Film Photodetector by Strain Gradient in van Der Waals Effective Homojunctions. *Adv. Opt. Mater.* **2021**, *9*, 2101310. [CrossRef]
133. Gan, X.; Shiue, R.-J.; Gao, Y.; Meric, I.; Heinz, T.F.; Shepard, K.; Hone, J.; Assefa, S.; Englund, D. Chip-Integrated Ultrafast Graphene Photodetector with High Responsivity. *Nat. Photonics* **2013**, *7*, 883–887. [CrossRef]
134. Kim, C.O.; Kim, S.; Shin, D.H.; Kang, S.S.; Kim, J.M.; Jang, C.W.; Joo, S.S.; Lee, J.S.; Kim, J.H.; Choi, S.-H.; et al. High Photoresponsivity in an All-Graphene p–n Vertical Junction Photodetector. *Nat. Commun.* **2014**, *5*, 3249. [CrossRef]
135. Schuler, S.; Schall, D.; Neumaier, D.; Schwarz, B.; Watanabe, K.; Taniguchi, T.; Mueller, T. Graphene Photodetector Integrated on a Photonic Crystal Defect Waveguide. *ACS Photonics* **2018**, *5*, 4758–4763. [CrossRef]
136. Ma, P.; Salamin, Y.; Baeuerle, B.; Josten, A.; Heni, W.; Emboras, A.; Leuthold, J. Plasmonically Enhanced Graphene Photodetector Featuring 100 Gbit/s Data Reception, High Responsivity, and Compact Size. *ACS Photonics* **2019**, *6*, 154–161. [CrossRef]
137. AlAloul, M.; Rasras, M. Plasmon-Enhanced Graphene Photodetector with CMOS-Compatible Titanium Nitride. *J. Opt. Soc. Am. B* **2021**, *38*, 602. [CrossRef]
138. Sulas-Kern, D.B.; Miller, E.M.; Blackburn, J.L. Photoinduced Charge Transfer in Transition Metal Dichalcogenide Heterojunctions—Towards next Generation Energy Technologies. *Energy Environ. Sci.* **2020**, *13*, 2684–2740. [CrossRef]
139. Ma, Y.; Dai, Y.; Guo, M.; Niu, C.; Lu, J.; Huang, B. Electronic and Magnetic Properties of Perfect, Vacancy-Doped, and Nonmetal Adsorbed $MoSe_2$, $MoTe_2$ and $WS_2$ Monolayers. *Phys. Chem. Chem. Phys.* **2011**, *13*, 15546. [CrossRef]
140. Fathipour, S.; Ma, N.; Hwang, W.S.; Protasenko, V.; Vishwanath, S.; Xing, H.G.; Xu, H.; Jena, D.; Appenzeller, J.; Seabaugh, A. Exfoliated Multilayer $MoTe_2$ Field-Effect Transistors. *Appl. Phys. Lett.* **2014**, *105*, 192101. [CrossRef]
141. Huang, H.; Wang, J.; Hu, W.; Liao, L.; Wang, P.; Wang, X.; Gong, F.; Chen, Y.; Wu, G.; Luo, W.; et al. Highly Sensitive Visible to Infrared $MoTe_2$ Photodetectors Enhanced by the Photogating Effect. *Nanotechnology* **2016**, *27*, 445201. [CrossRef]
142. Tran, V.; Soklaski, R.; Liang, Y.; Yang, L. Layer-Controlled Band Gap and Anisotropic Excitons in Few-Layer Black Phosphorus. *Phys. Rev. B* **2014**, *89*, 235319. [CrossRef]
143. Jalaei, S.; Karamdel, J.; Ghalami-Bavil-Olyaee, H. Mid-Infrared Photodetector Based on Selenium-Doped Black Phosphorus. *Phys. Status Solidi A* **2020**, *217*, 2000483. [CrossRef]
144. Fu, Q.; Wang, X.; Liu, F.; Dong, Y.; Liu, Z.; Zheng, S.; Chaturvedi, A.; Zhou, J.; Hu, P.; Zhu, Z.; et al. Ultrathin Ruddlesden–Popper Perovskite Heterojunction for Sensitive Photodetection. *Small* **2019**, *15*, 1902890. [CrossRef] [PubMed]
145. Kim, H.-S.; Lee, C.-R.; Im, J.-H.; Lee, K.-B.; Moehl, T.; Marchioro, A.; Moon, S.-J.; Humphry-Baker, R.; Yum, J.-H.; Moser, J.E.; et al. Lead Iodide Perovskite Sensitized All-Solid-State Submicron Thin Film Mesoscopic Solar Cell with Efficiency Exceeding 9%. *Sci. Rep.* **2012**, *2*, 591. [CrossRef] [PubMed]
146. Lee, M.M.; Teuscher, J.; Miyasaka, T.; Murakami, T.N.; Snaith, H.J. Efficient Hybrid Solar Cells Based on Meso-Superstructured Organometal Halide Perovskites. *Science* **2012**, *338*, 643–647. [CrossRef]
147. Burschka, J.; Pellet, N.; Moon, S.-J.; Humphry-Baker, R.; Gao, P.; Nazeeruddin, M.K.; Grätzel, M. Sequential Deposition as a Route to High-Performance Perovskite-Sensitized Solar Cells. *Nature* **2013**, *499*, 316–319. [CrossRef]

148. Yang, W.S.; Noh, J.H.; Jeon, N.J.; Kim, Y.C.; Ryu, S.; Seo, J.; Seok, S.I. High-Performance Photovoltaic Perovskite Layers Fabricated through Intramolecular Exchange. *Science* **2015**, *348*, 1234–1237. [CrossRef]
149. Bi, C.; Wang, Q.; Shao, Y.; Yuan, Y.; Xiao, Z.; Huang, J. Non-Wetting Surface-Driven High-Aspect-Ratio Crystalline Grain Growth for Efficient Hybrid Perovskite Solar Cells. *Nat. Commun.* **2015**, *6*, 7747. [CrossRef]
150. Serpetzoglou, E.; Konidakis, I.; Kakavelakis, G.; Maksudov, T.; Kymakis, E.; Stratakis, E. Improved Carrier Transport in Perovskite Solar Cells Probed by Femtosecond Transient Absorption Spectroscopy. *ACS Appl. Mater. Interfaces* **2017**, *9*, 43910–43919. [CrossRef]
151. Li, F.; Zhu, W.; Bao, C.; Yu, T.; Wang, Y.; Zhou, X.; Zou, Z. Laser-Assisted Crystallization of $CH_3NH_3PbI_3$ Films for Efficient Perovskite Solar Cells with a High Open-Circuit Voltage. *Chem. Commun.* **2016**, *52*, 5394–5397. [CrossRef]
152. Jeon, T.; Jin, H.M.; Lee, S.H.; Lee, J.M.; Park, H.I.; Kim, M.K.; Lee, K.J.; Shin, B.; Kim, S.O. Laser Crystallization of Organic–Inorganic Hybrid Perovskite Solar Cells. *ACS Nano* **2016**, *10*, 7907–7914. [CrossRef]
153. Konidakis, I.; Maksudov, T.; Serpetzoglou, E.; Kakavelakis, G.; Kymakis, E.; Stratakis, E. Improved Charge Carrier Dynamics of $CH_3NH_3PbI_3$ Perovskite Films Synthesized by Means of Laser-Assisted Crystallization. *ACS Appl. Energy Mater.* **2018**, *1*, 5101–5111. [CrossRef]
154. Jung, E.H.; Jeon, N.J.; Park, E.Y.; Moon, C.S.; Shin, T.J.; Yang, T.-Y.; Noh, J.H.; Seo, J. Efficient, Stable and Scalable Perovskite Solar Cells Using Poly(3-Hexylthiophene). *Nature* **2019**, *567*, 511–515. [CrossRef]
155. Yan, J.; Qiu, W.; Wu, G.; Heremans, P.; Chen, H. Recent Progress in 2D/Quasi-2D Layered Metal Halide Perovskites for Solar Cells. *J. Mater. Chem. A* **2018**, *6*, 11063–11077. [CrossRef]
156. Liu, P.; Han, N.; Wang, W.; Ran, R.; Zhou, W.; Shao, Z. High-Quality Ruddlesden–Popper Perovskite Film Formation for High-Performance Perovskite Solar Cells. *Adv. Mater.* **2021**, *33*, 2002582. [CrossRef] [PubMed]
157. Shao, S.; Duim, H.; Wang, Q.; Xu, B.; Dong, J.; Adjokatse, S.; Blake, G.R.; Protesescu, L.; Portale, G.; Hou, J.; et al. Tuning the Energetic Landscape of Ruddlesden–Popper Perovskite Films for Efficient Solar Cells. *ACS Energy Lett.* **2020**, *5*, 39–46. [CrossRef]
158. Yang, R.; Li, R.; Cao, Y.; Wei, Y.; Miao, Y.; Tan, W.L.; Jiao, X.; Chen, H.; Zhang, L.; Chen, Q.; et al. Oriented Quasi-2D Perovskites for High Performance Optoelectronic Devices. *Adv. Mater.* **2018**, *30*, 1804771. [CrossRef]
159. Chen, K.; Jin, W.; Zhang, Y.; Yang, T.; Reiss, P.; Zhong, Q.; Bach, U.; Li, Q.; Wang, Y.; Zhang, H.; et al. High Efficiency Mesoscopic Solar Cells Using $CsPbI_3$ Perovskite Quantum Dots Enabled by Chemical Interface Engineering. *J. Am. Chem. Soc.* **2020**, *142*, 3775–3783. [CrossRef]
160. Yuan, J.; Hazarika, A.; Zhao, Q.; Ling, X.; Moot, T.; Ma, W.; Luther, J.M. Metal Halide Perovskites in Quantum Dot Solar Cells: Progress and Prospects. *Joule* **2020**, *4*, 1160–1185. [CrossRef]
161. Bao, C.; Yang, J.; Bai, S.; Xu, W.; Yan, Z.; Xu, Q.; Liu, J.; Zhang, W.; Gao, F. High Performance and Stable All-Inorganic Metal Halide Perovskite-Based Photodetectors for Optical Communication Applications. *Adv. Mater.* **2018**, *30*, 1803422. [CrossRef]
162. Leung, S.-F.; Ho, K.-T.; Kung, P.-K.; Hsiao, V.K.S.; Alshareef, H.N.; Wang, Z.L.; He, J.-H. A Self-Powered and Flexible Organometallic Halide Perovskite Photodetector with Very High Detectivity. *Adv. Mater.* **2018**, *30*, 1704611. [CrossRef]
163. Xu, Z.; Li, Y.; Liu, X.; Ji, C.; Chen, H.; Li, L.; Han, S.; Hong, M.; Luo, J.; Sun, Z. Highly Sensitive and Ultrafast Responding Array Photodetector Based on a Newly Tailored 2D Lead Iodide Perovskite Crystal. *Adv. Opt. Mater.* **2019**, *7*, 1900308. [CrossRef]
164. Loi, H.; Cao, J.; Guo, X.; Liu, C.; Wang, N.; Song, J.; Tang, G.; Zhu, Y.; Yan, F. Gradient 2D/3D Perovskite Films Prepared by Hot-Casting for Sensitive Photodetectors. *Adv. Sci.* **2020**, *7*, 2000776. [CrossRef] [PubMed]
165. Ma, X.; Xu, Y.; Li, S.; Lo, T.W.; Zhang, B.; Rogach, A.L.; Lei, D. A Flexible Plasmonic-Membrane-Enhanced Broadband Tin-Based Perovskite Photodetector. *Nano Lett.* **2021**, *21*, 9195–9202. [CrossRef]
166. Qian, L.; Sun, Y.; Sun, M.; Fang, Z.; Li, L.; Xie, D.; Li, C.; Ding, L. 2D Perovskite Microsheets for High-Performance Photodetectors. *J. Mater. Chem. C* **2019**, *7*, 5353–5358. [CrossRef]
167. Qian, L.; Sun, Y.; Wu, M.; Li, C.; Xie, D.; Ding, L.; Shi, G. A Lead-Free Two-Dimensional Perovskite for a High-Performance Flexible Photoconductor and a Light-Stimulated Synaptic Device. *Nanoscale* **2018**, *10*, 6837–6843. [CrossRef] [PubMed]
168. Zhang, X.; Wang, Q.; Jin, Z.; Zhang, J.; Liu, S. (Frank) Stable Ultra-Fast Broad-Bandwidth Photodetectors Based on $\alpha$-$CsPbI_3$ Perovskite and $NaYF_4$:Yb,Er Quantum Dots. *Nanoscale* **2017**, *9*, 6278–6285. [CrossRef] [PubMed]
169. Chen, H.; Hou, Y.; Halbig, C.E.; Chen, S.; Zhang, H.; Li, N.; Guo, F.; Tang, X.; Gasparini, N.; Levchuk, I.; et al. Extending the Environmental Lifetime of Unpackaged Perovskite Solar Cells through Interfacial Design. *J. Mater. Chem. A* **2016**, *4*, 11604–11610. [CrossRef]
170. Singh, R.; Giri, A.; Pal, M.; Thiyagarajan, K.; Kwak, J.; Lee, J.-J.; Jeong, U.; Cho, K. Perovskite Solar Cells with an $MoS_2$ Electron Transport Layer. *J. Mater. Chem. A* **2019**, *7*, 7151–7158. [CrossRef]
171. Sherkar, T.S.; Momblona, C.; Gil-Escrig, L.; Ávila, J.; Sessolo, M.; Bolink, H.J.; Koster, L.J.A. Recombination in Perovskite Solar Cells: Significance of Grain Boundaries, Interface Traps, and Defect Ions. *ACS Energy Lett.* **2017**, *2*, 1214–1222. [CrossRef]
172. Wang, Y.; Hu, Y.; Han, D.; Yuan, Q.; Cao, T.; Chen, N.; Zhou, D.; Cong, H.; Feng, L. Ammonia-Treated Graphene Oxide and PEDOT:PSS as Hole Transport Layer for High-Performance Perovskite Solar Cells with Enhanced Stability. *Org. Electron.* **2019**, *70*, 63–70. [CrossRef]
173. Yun, J.-M.; Yeo, J.-S.; Kim, J.; Jeong, H.-G.; Kim, D.-Y.; Noh, Y.-J.; Kim, S.-S.; Ku, B.-C.; Na, S.-I. Solution-Processable Reduced Graphene Oxide as a Novel Alternative to PEDOT:PSS Hole Transport Layers for Highly Efficient and Stable Polymer Solar Cells. *Adv. Mater.* **2011**, *23*, 4923–4928. [CrossRef] [PubMed]

174. Yeo, J.-S.; Kang, R.; Lee, S.; Jeon, Y.-J.; Myoung, N.; Lee, C.-L.; Kim, D.-Y.; Yun, J.-M.; Seo, Y.-H.; Kim, S.-S.; et al. Highly Efficient and Stable Planar Perovskite Solar Cells with Reduced Graphene Oxide Nanosheets as Electrode Interlayer. *Nano Energy* **2015**, *12*, 96–104. [CrossRef]
175. Jokar, E.; Huang, Z.Y.; Narra, S.; Wang, C.-Y.; Kattoor, V.; Chung, C.-C.; Diau, E.W.-G. Anomalous Charge-Extraction Behavior for Graphene-Oxide (GO) and Reduced Graphene-Oxide (RGO) Films as Efficient p-Contact Layers for High-Performance Perovskite Solar Cells. *Adv. Energy Mater.* **2018**, *8*, 1701640. [CrossRef]
176. Agresti, A.; Pescetelli, S.; Cinà, L.; Konios, D.; Kakavelakis, G.; Kymakis, E.; Carlo, A.D. Efficiency and Stability Enhancement in Perovskite Solar Cells by Inserting Lithium-Neutralized Graphene Oxide as Electron Transporting Layer. *Adv. Funct. Mater.* **2016**, *26*, 2686–2694. [CrossRef]
177. Batmunkh, M.; Vimalanathan, K.; Wu, C.; Bati, A.S.R.; Yu, L.; Tawfik, S.A.; Ford, M.J.; Macdonald, T.J.; Raston, C.L.; Priya, S.; et al. Efficient Production of Phosphorene Nanosheets via Shear Stress Mediated Exfoliation for Low-Temperature Perovskite Solar Cells. *Small Methods* **2019**, *3*, 1800521. [CrossRef]
178. Zhao, X.; Liu, S.; Zhang, H.; Chang, S.-Y.; Huang, W.; Zhu, B.; Shen, Y.; Shen, C.; Wang, D.; Yang, Y.; et al. 20% Efficient Perovskite Solar Cells with 2D Electron Transporting Layer. *Adv. Funct. Mater.* **2019**, *29*, 1805168. [CrossRef]
179. Kim, Y.G.; Kwon, K.C.; Le, Q.V.; Hong, K.; Jang, H.W.; Kim, S.Y. Atomically Thin Two-Dimensional Materials as Hole Extraction Layers in Organolead Halide Perovskite Photovoltaic Cells. *J. Power Sources* **2016**, *319*, 1–8. [CrossRef]
180. Chen, L.-C.; Tseng, Z.-L.; Chen, C.-C.; Chang, S.H.; Ho, C.-H. Fabrication and Characteristics of $CH_3$ $NH_3$ $PbI_3$ Perovskite Solar Cells with Molybdenum-Selenide Hole-Transport Layer. *Appl. Phys. Express* **2016**, *9*, 122301. [CrossRef]
181. Yang, L.; Dall'Agnese, C.; Dall'Agnese, Y.; Chen, G.; Gao, Y.; Sanehira, Y.; Jena, A.K.; Wang, X.; Gogotsi, Y.; Miyasaka, T. Surface-Modified Metallic $Ti_3C_2T_x$ MXene as Electron Transport Layer for Planar Heterojunction Perovskite Solar Cells. *Adv. Funct. Mater.* **2019**, *29*, 1905694. [CrossRef]
182. Furchi, M.; Urich, A.; Pospischil, A.; Lilley, G.; Unterrainer, K.; Detz, H.; Klang, P.; Andrews, A.M.; Schrenk, W.; Strasser, G.; et al. Microcavity-Integrated Graphene Photodetector. *Nano Lett.* **2012**, *12*, 2773–2777. [CrossRef] [PubMed]
183. Konstantatos, G.; Badioli, M.; Gaudreau, L.; Osmond, J.; Bernechea, M.; de Arquer, F.P.G.; Gatti, F.; Koppens, F.H.L. Hybrid Graphene–Quantum Dot Phototransistors with Ultrahigh Gain. *Nat. Nanotechnol.* **2012**, *7*, 363–368. [CrossRef] [PubMed]
184. Lee, Y.; Kwon, J.; Hwang, E.; Ra, C.-H.; Yoo, W.J.; Ahn, J.-H.; Park, J.H.; Cho, J.H. High-Performance Perovskite-Graphene Hybrid Photodetector. *Adv. Mater.* **2015**, *27*, 41–46. [CrossRef] [PubMed]
185. Zou, Y.; Zou, T.; Zhao, C.; Wang, B.; Xing, J.; Yu, Z.; Cheng, J.; Xin, W.; Yang, J.; Yu, W.; et al. A Highly Sensitive Single Crystal Perovskite–Graphene Hybrid Vertical Photodetector. *Small* **2020**, *16*, 2000733. [CrossRef]
186. Bera, K.P.; Haider, G.; Huang, Y.-T.; Roy, P.K.; Paul Inbaraj, C.R.; Liao, Y.-M.; Lin, H.-I.; Lu, C.-H.; Shen, C.; Shih, W.Y.; et al. Graphene Sandwich Stable Perovskite Quantum-Dot Light-Emissive Ultrasensitive and Ultrafast Broadband Vertical Phototransistors. *ACS Nano* **2019**, *13*, 12540–12552. [CrossRef]
187. Chen, Z.; Kang, Z.; Rao, C.; Cheng, Y.; Liu, N.; Zhang, Z.; Li, L.; Gao, Y. Improving Performance of Hybrid Graphene–Perovskite Photodetector by a Scratch Channel. *Adv. Electron. Mater.* **2019**, *5*, 1900168. [CrossRef]
188. Lu, J.; Carvalho, A.; Liu, H.; Lim, S.X.; Castro Neto, A.H.; Sow, C.H. Hybrid Bilayer $WSe_2$-$CH_3NH_3PbI_3$ Organolead Halide Perovskite as a High-Performance Photodetector. *Angew. Chem.* **2016**, *128*, 12124–12128. [CrossRef]
189. Wang, Y.; Fullon, R.; Acerce, M.; Petoukhoff, C.E.; Yang, J.; Chen, C.; Du, S.; Lai, S.K.; Lau, S.P.; Voiry, D.; et al. Solution-Processed $MoS_2$/Organolead Trihalide Perovskite Photodetectors. *Adv. Mater.* **2017**, *29*, 1603995. [CrossRef]
190. Erkılıç, U.; Solís-Fernández, P.; Ji, H.G.; Shinokita, K.; Lin, Y.-C.; Maruyama, M.; Suenaga, K.; Okada, S.; Matsuda, K.; Ago, H. Vapor Phase Selective Growth of Two-Dimensional Perovskite/$WS_2$ Heterostructures for Optoelectronic Applications. *ACS Appl. Mater. Interfaces* **2019**, *11*, 40503–40511. [CrossRef]
191. Wu, H.; Si, H.; Zhang, Z.; Kang, Z.; Wu, P.; Zhou, L.; Zhang, S.; Zhang, Z.; Liao, Q.; Zhang, Y. All-Inorganic Perovskite Quantum Dot-Monolayer $MoS_2$ Mixed-Dimensional van Der Waals Heterostructure for Ultrasensitive Photodetector. *Adv. Sci.* **2018**, *5*, 1801219. [CrossRef]
192. Wang, L.; Zou, X.; Lin, J.; Jiang, J.; Liu, Y.; Liu, X.; Zhao, X.; Liu, Y.F.; Ho, J.C.; Liao, L. Perovskite/Black Phosphorus/$MoS_2$ Photogate Reversed Photodiodes with Ultrahigh Light On/Off Ratio and Fast Response. *ACS Nano* **2019**, *13*, 4804–4813. [CrossRef] [PubMed]
193. Muduli, S.; Pandey, P.; Devatha, G.; Babar, R.; Thripuranthaka, M.; Kothari, D.C.; Kabir, M.; Pillai, P.P.; Ogale, S. Photoluminescence Quenching in Self-Assembled $CsPbBr_3$ Quantum Dots on Few-Layer Black Phosphorus Sheets. *Angew. Chem.* **2018**, *130*, 7808–7812. [CrossRef]
194. Deng, W.; Huang, H.; Jin, H.; Li, W.; Chu, X.; Xiong, D.; Yan, W.; Chun, F.; Xie, M.; Luo, C.; et al. All-Sprayed-Processable, Large-Area, and Flexible Perovskite/MXene-Based Photodetector Arrays for Photocommunication. *Adv. Opt. Mater.* **2019**, *7*, 1801521. [CrossRef]
195. Liang, C.; Zhao, D.; Li, Y.; Li, X.; Peng, S.; Shao, G.; Xing, G. Ruddlesden-Popper Perovskite for Stable Solar Cells. *Energy Environ. Mater.* **2018**, *1*, 221–231. [CrossRef]
196. Lin, Y.; Bai, Y.; Fang, Y.; Wang, Q.; Deng, Y.; Huang, J. Suppressed Ion Migration in Low-Dimensional Perovskites. *ACS Energy Lett.* **2017**, *2*, 1571–1572. [CrossRef]
197. Xu, Z.; Lu, D.; Dong, X.; Chen, M.; Fu, Q.; Liu, Y. Highly Efficient and Stable Dion−Jacobson Perovskite Solar Cells Enabled by Extended Π-Conjugation of Organic Spacer. *Adv. Mater.* **2021**, *33*, 2105083. [CrossRef]

198. Zhang, Q.; Wang, B.; Zheng, W.; Kong, L.; Wan, Q.; Zhang, C.; Li, Z.; Cao, X.; Liu, M.; Li, L. Ceramic-like Stable $CsPbBr_3$ Nanocrystals Encapsulated in Silica Derived from Molecular Sieve Templates. *Nat. Commun.* **2020**, *11*, 31. [CrossRef]
199. Tan, C.; Chen, J.; Wu, X.-J.; Zhang, H. Epitaxial Growth of Hybrid Nanostructures. *Nat. Rev. Mater.* **2018**, *3*, 17089. [CrossRef]
200. Huang, G.; Wang, C.; Xu, S.; Zong, S.; Lu, J.; Wang, Z.; Lu, C.; Cui, Y. Postsynthetic Doping of $MnCl_2$ Molecules into Preformed $CsPbBr_3$ Perovskite Nanocrystals via a Halide Exchange-Driven Cation Exchange. *Adv. Mater.* **2017**, *29*, 1700095. [CrossRef]
201. Zhang, L.; Kang, C.; Zhang, G.; Pan, Z.; Huang, Z.; Xu, S.; Rao, H.; Liu, H.; Wu, S.; Wu, X.; et al. All-Inorganic $CsPbI_3$ Quantum Dot Solar Cells with Efficiency over 16% by Defect Control. *Adv. Funct. Mater.* **2021**, *31*, 2005930. [CrossRef]
202. Liu, F.; Ding, C.; Zhang, Y.; Ripolles, T.S.; Kamisaka, T.; Toyoda, T.; Hayase, S.; Minemoto, T.; Yoshino, K.; Dai, S.; et al. Colloidal Synthesis of Air-Stable Alloyed $CsSn_{1-x}Pb_xI_3$ Perovskite Nanocrystals for Use in Solar Cells. *J. Am. Chem. Soc.* **2017**, *139*, 16708–16719. [CrossRef] [PubMed]